

# Thermal Feedback in the high-mass star and cluster forming region W51

Adam Ginsburg<sup>1,2</sup>, Ciriaco Goddi<sup>3,4</sup>, Roberto Galván-Madrid<sup>5</sup>, John Bally<sup>7</sup>, Rowan Smith\*, Jeremy Darling<sup>7</sup>, J. M. Diederik Kruijssen\*, Erik Rosolowsky \*, Robert Loughnane<sup>5</sup>, Leonardo Testi<sup>1,\*,\*</sup>, Nate Bastian \*, Jaime E. Pineda \*, Elisabeth Mills \*

<sup>1</sup> European Southern Observatory, Karl-Schwarzschild-Straße 2, D-85748 Garching bei München, Germany

e-mail: Adam.Ginsburg@eso.org

<sup>2</sup> National Radio Astronomy Observatory, Socorro, NM 87801 USA

\* Max-Planck-Institut für extraterrestrische Physik, Giessenbachstrasse 1, 85748 Garching, Germany

\* INAF-Osservatorio Astrofisico di Arcetri, Largo E. Fermi 5, I-50125, Florence, Italy

\* Excellence Cluster Universe, Boltzman str. 2, D-85748 Garching bei München, Germany

<sup>3</sup> Department of Astrophysics/IMAPP, Radboud University Nijmegen, PO Box 9010, 6500 GL Nijmegen, the Netherlands

<sup>4</sup> ALLEGRO/Leiden Observatory, Leiden University, PO Box 9513, 2300 RA Leiden, the Netherlands

<sup>5</sup> Instituto de Radioastronomía y Astrofísica, UNAM, A.P. 3-72, Xangari, Morelia, 58089, Mexico

<sup>7</sup> CASA, University of Colorado, 389-UCB, Boulder, CO 80309

\* Jodrell Bank Centre for Astrophysics, School of Physics and Astronomy, University of Manchester, Oxford Road, Manchester M13 9PL, UK

\* Astronomisches Rechen-Institut, Zentrum für Astronomie der Universität Heidelberg, Mönchhofstraße 12-14, 69120 Heidelberg, Germany

\* Dept. of Physics, University of Alberta, Edmonton, Alberta, Canada

\* Astrophysics Research Institute, Liverpool John Moores University, 146 Brownlow Hill, Liverpool L3 5RF, UK

\* UCSD TODO finish this

2016/10/31

## ABSTRACT

We present ALMA observations of a  $\sim 3 \times 1.5$  pc area in the W51 high-mass star-forming complex. We identify dust continuum sources and measure the gas and dust temperature through both rotational diagram modeling and brightness-temperature-based limits. The observed region contains three high-mass YSOs that appear to be at the earliest stages of their formation, with no signs of ionizing radiation from their central sources. The new data reveal high gas and dust temperatures ( $T > 100$  K) extending out to about 5000 AU from each of these sources, indicating that the forming MYSOs are able to heat a large volume of gas in which fragmentation is suppressed. No distinct fragments are observed within this heated zone, though 75 sources representing either prestellar cores or some stage of protostars are detected in the observed field. During the process of forming, high-mass stars heat a large volume (and correspondingly large mass) of gas, preventing it from fragmenting, and therefore keep a large reservoir available to feed from. By contrast, more mature massive stars that illuminate compact H II regions have little effect on their surrounding dense gas, hinting that these sources have completed most or all of their accretion.

## 1. Introduction

High-mass stars are the drivers of galaxy evolution, cycling enriched materials into the interstellar medium (ISM) and illuminating it. During their formation process, however, these stars are nearly undetectable because of their rarity and their opaque surroundings. We therefore know relatively little about how massive stars acquire their mass and what their immediate surroundings look like at this early time.

Assuming the stellar initial mass function (IMF) is a universal (or nearly universal) distribution, massive stars O-stars (with  $M > 50M_{\odot}$ ) almost always form in a clustered fashion (in proto-clusters or proto-associations). Their presence, and the strong feedback they produce, may directly influence how the IMF around them is formed. If feedback from these stars is relevant while most of the mass surrounding them is still in gas (not yet in stars), the mass

function in such clusters cannot be determined by ISM properties alone.

Models of high-mass star formation universally have difficulty collapsing enough material to a stellar radius to form very massive stars. Generally, these models produce a high-mass star with enough luminosity to halt further *spherical* accretion at a very early stage, with  $M_* \sim 10 - 20M_{\odot}$ . Radiation pressure provides a fundamental limit on how much mass can be accreted, but geometric effects can circumvent this limit and allow further accretion (Yorke & Sonnhalter 2002; Krumholz et al. 2005, 2009; Krumholz & Matzner 2009; Kuiper & Yorke 2012, 2013; Rosen et al. 2016). Additionally, fragmentation-induced starvation can limit the amount of mass available to the most massive star, instead breaking up massive cores into many lower-mass fragments (Peters et al. 2010b). These simulations still have limited physics and can only produce stars up to  $M \sim 80 M_{\odot}$  even in the current best cases (Kuiper et al. 2015, 2016). The question of how massive stars acquire their mass, and es-

pecially whether they ever form Keplerian disks, remains open (Beltrán & de Wit 2016).

Nature is clearly capable of producing massive stars and some that are much larger than those produced in simulations. For example, within the LMC, stars up to  $M \sim 300 M_{\odot}$  have been spectroscopically identified (Crowther et al. 2016), so we know it is possible to form these. Within our own Galaxy, UV and optical characterization of these stars is not possible, but some infrared lines are indicators of such stars. Barbosa et al. (2008) identified an O3 and an O4 star ( $M \gtrsim 50 M_{\odot}$ ) within the W51 IRS2 region, demonstrating that this region has at some time been capable of forming such stars.

The W51 cloud contains two protocluster regions, IRS2 and e1/e2, which each contain  $M \gtrsim 10^4 M_{\odot}$  of gas and have far-infrared luminosities that indicate the presence of formed or forming massive stars (Harvey et al. 1986; Sievers et al. 1991; Ginsburg et al. 2012, 2016b). Previous millimeter and centimeter observations have revealed the gas that is forming new stars and indicated that the new stars are likely to be massive (Zhang & Ho 1997; Eisner et al. 2002; Zapata et al. 2009, 2010; Shi et al. 2010a,b; Goddi et al. 2016). The W51 protoclusters, while distant (5.4 kpc; Sato et al. 2010), therefore provide a powerful laboratory for studying high-mass star formation in an environment where massive star feedback is already evident, but formation is still ongoing.

This combination of feedback and ongoing formation is essential for testing components of high mass star formation theory that are relatively inaccessible to simulations. Krumholz (2006) suggests that accretion heating during the formation of high-mass stars can heat massive cores to  $\gtrsim 100$  K and therefore suppress fragmentation into smaller stars, which would be expected for cold cores. While simulations have verified the conclusion that early-stage accretion heating can control the mass scale within low-mass star forming regions (Krumholz et al. 2007; Offner et al. 2011; Bate 2012; Bate et al. 2014), there have been neither theoretical nor observational tests of this model for high-mass stars.

**The major sectioning/subsectioning breakdown is awkward.** We present an observational study of the high-mass star-forming region W51. In Section 2, we describe the observations and data reduction process. Section 3 describes the analysis, including source identification (§3.1), spatial distribution (§3.2), and photometry (§3.3). We then examine the source temperatures (§3.4) in order to determine their nature (§3.5). We examine the most massive cores in Sections 3.5.1 and 3.5.2 and then compute their radial mass profiles in 3.6. Section 3.7 describes the mass and flux recovered on different spatial scales, Section 3.8 the observed chemical distribution, and Section 3.9 the temperatures inferred from CH<sub>3</sub>OH lines (§3.9). Section 3.10 shows that the heating is not coming from H II regions. Section 3.11 and its subsections describe outflows Section 4 discusses scales and types of feedback (§4.1), outflows (§4.1.2), accretion and outflows (§4.2), and fragmentation (§4.3). We conclude in Section 5. Additional interesting features in the W51 data not directly relevant to our main topic are discussed in Appendix A.

## 2. Observations

As part of ALMA Cycle 2 program 2013.1.00308.S, we observed a  $\sim 2' \times 1'$  region centered between W51 IRS2 and W51 e1/e2 with a 37-pointing mosaic. Two configurations of the 12m array were used, achieving a resolution of  $0.2''$ . Additionally, a 12-pointing mosaic was performed using the 7m array, hypothetically probing scales up to  $\sim 28''$ . The full UV coverage was from  $\sim 12$  to  $\sim 1500$  m (figure 2).

Additionally, we will comment briefly on project 2015.1.01569.S (PI: Goddi), which observed two fields centered on e2e/e8 and north with very long baselines (resolution  $0.04''$ ) and provide additional insights that our  $0.2''$  data do not yield alone. Full details of that data set will be released in a future work.

### 2.1. Data Reduction

Data reduction was performed using CASA. The QA2-produced data products were combined using the standard inverse variance weighting. Two sets of images were produced for different aspects of the analysis, one including the 7m array data and one including only 12m data. Except where otherwise noted, the 12m-only data were used in order to focus on the compact structures.

Full details of the data reduction, including all scripts used, can be found on the project's github repository<sup>1</sup>.

#### 2.1.1. Continuum

A continuum image combining all 4 spectral windows was produced using `tclean`. We phase self-calibrated the data on baselines longer than 100m to increase the dynamic range. The final image was cleaned with 50000 iterations to a threshold of 5 mJy. The lowest noise level in the image, away from bright sources, is  $\sim 0.2$  mJy/beam, but near the bright sources e2 and IRS2, the noise reached as high as  $\sim 2$  mJy/beam. Deeper cleaning was attempted, but lead to instabilities. The combined image has a central frequency of about 226.6 GHz assuming a flat spectrum soure.

#### 2.1.2. Lines

We produced spectral image cubes of the lines listed in Tables 2, 3, 4, and 5. For kinematic and moment analysis, the median value over the spectral range [25,30],[80,95] km s<sup>-1</sup> was used to estimate and subtract the local continuum.

## 3. Results & Analysis

### 3.1. Source Identification

We used the `dendrogram` method described by Rosolowsky et al. (2008) and implemented in `astrodendro` to identify sources. We used a minimum value of 1 mJy/beam ( $\sim 5 - \sigma$ ) and a minimum  $\Delta = 0.4$  mJy/beam ( $\sim 2 - \sigma$ ) with minimum 10 pixels (each pixel is  $0.05''$ ). This cataloging yielded over 8000 candidate sources, of which the majority are noise or artifacts around the brightest sources. To filter out these bad sources, we created a noise map taking the local RMS of the `tclean`-produced residual map over a  $\sigma = 30$  pixel ( $1.5''$ ) gaussian. We then removed all sources with peak

<sup>1</sup> [https://github.com/keflavich/W51\\_ALMA\\_2013.1.00308.S](https://github.com/keflavich/W51_ALMA_2013.1.00308.S)



**Fig. 1.** An overview of the W51A region as seen by ALMA. The grayscale shows a 1.3mm ALMA image. [This is a placeholder](#)

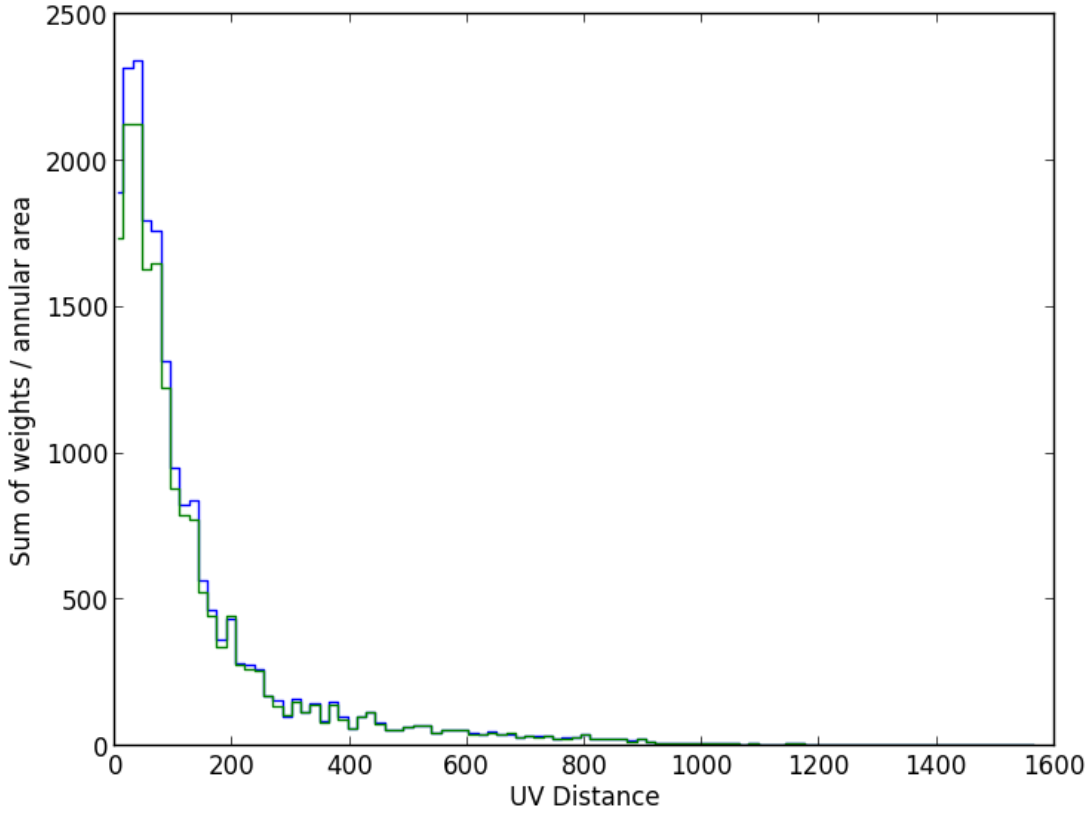


**Fig. 2.** A weighted histogram of the visibility weights as a function of UV distance; this approximately shows the amount of data received at each baseline length.

$S/N < 8$ , mean  $S/N$  per pixel  $< 5$ , and minimum  $S/N$  per pixel  $< 1$ . We also only included the smallest sources in the dendrogram, the “leaves”. These parameters were tuned by checking against “real” sources identified by eye and selected using ds9: most real sources are recovered and few

spurious sources ( $< 10$ ) are included. The resulting catalog includes 113 sources.

The ‘by-eye’ core extraction approach, in which we placed ds9 regions on all sources that look ‘real’, produced a more reliable but less complete (and less quantifiable) catalog containing 75 sources. This catalog is more useful in the

**Table 1.** Spectral Setup

| SpwID | Minimum Frequency<br>GHz | Maximum Frequency<br>GHz | Channel Width<br>kHz |
|-------|--------------------------|--------------------------|----------------------|
| 0     | 218.11930228             | 218.619301               | -122.07              |
| 1     | 218.36288652             | 220.355073               | -488.281             |
| 2     | 230.376575               | 232.36876148             | 488.281              |
| 3     | 232.981075               | 234.97326148             | 488.281              |

**Table 2.** Spectral Lines in SPW 0

| Line Name   | Frequency<br>GHz |
|---|------------------|
| H <sub>2</sub> CO 3 <sub>0,3</sub> – 2 <sub>0,2</sub>                       | 218.22219        |
| H <sub>2</sub> CO 3 <sub>2,2</sub> – 2 <sub>2,1</sub>                       | 218.47564        |
| CH <sub>3</sub> OH 4 <sub>2,2</sub> – 3 <sub>1,2</sub>                      | 218.44005        |
| CH <sub>3</sub> OCHO 17 <sub>3,14</sub> – 16 <sub>3,13</sub> E              | 218.28083        |
| CH <sub>3</sub> OCHO 17 <sub>3,14</sub> – 16 <sub>3,13</sub> A              | 218.29787        |
| CH <sub>3</sub> CH <sub>2</sub> CN 24 <sub>3,21</sub> – 23 <sub>3,20</sub>  | 218.39002        |
| Acetone 8 <sub>7,1</sub> – 7 <sub>4,4</sub> AE                              | 218.24017        |
| O <sup>13</sup> CS 18-17  | 218.19898        |
| CH <sub>3</sub> OCH <sub>3</sub> 23 <sub>3,21</sub> – 23 <sub>2,22</sub> AA | 218.49441        |
| CH <sub>3</sub> OCH <sub>3</sub> 23 <sub>3,21</sub> – 23 <sub>2,22</sub> EE | 218.49192        |
| CH <sub>3</sub> NCO 25 <sub>1,24</sub> – 24 <sub>1,23</sub>                 | 218.5418         |
| CH <sub>3</sub> SH 23 <sub>2</sub> – 23 <sub>1</sub>                        | 218.18612        |

regions around the bright sources e2 and north, since these regions are affected by substantial uncleared PSF sidelobe artifacts. In particular, the dendrogram catalog includes a number of sources around e2/e8 that, by eye, appear to be parts of continuous extended emission rather than local peaks; “streaking” artifacts in the reduced data result in their identification despite our threshold criteria. The dendrogram extraction also identified sources within the IRS 2 H<sub>II</sub> region that are not dust sources. Dendrogram extraction missed a few clear sources in the low-noise regions away from W51 Main and IRS 2 because the identification criteria were too conservative.

When extracting properties of the ‘by-eye’ sources, we used variable sized circular apertures, where the apertures were selected to include all of the detectable symmetric emission around a central peak up to a maximum radius  $r \sim 0.6''$ . This approach is necessary, as some of the sources are not centrally peaked and are therefore likely to be spatially resolved starless cores.

### 3.2. The spatial distribution of continuum sources

The detected continuum sources are not uniformly distributed across the observed region. The most notable feature in the spatial distribution is their alignment: most continuum sources collect along approximately linear features. This is especially evident in W51 IRS2, where the core density is very high and there is virtually no deviation from the line. The e8 filament is also notably linear, though there are a few sources detected just off the filament.

On a larger scale, the e8 filament points toward e2, apparently tracing a slightly longer filamentary structure. With some imagination, this might be extended along the entire northeast ridge to eventually connect in a broad half-circle with the IRS2 filament (Figure 3). This morphology hints at a possible sequential star formation event, where some central bubble has swept gas into these filaments.

However, this ring has no counterparts in ionized gas, and there is little reason to expect such circular symmetry from a real cloud, so the star forming circle may be merely a figment.

Whether it is physical or not, there is a notable lack of continuum sources within the circle. There is no lack of molecular gas, however, as both CO and H<sub>2</sub>CO emission fill the full field of view.

### 3.3. Photometry

We created a catalog of the hand-extracted sources including their peak and mean flux density, their centroid, and their geometric properties. For each source, we further extracted aperture photometry around the centroid in 6 apertures: 0.2, 0.4, 0.6, 0.8, 1.0, and 1.5''. We performed the same aperture photometry on the W51 Ku-band images from [Ginsburg et al. \(2016a\)](#) to estimate the free-free contribution to the observed flux density measurements. These measurements are reported in Table 7.

The source flux density distribution is shown in Figure 4. The most common nearest-neighbor separation between catalogued sources is  $\sim 0.3''$ , which implies that the larger apertures double-count some pixels. The smallest separation is 0.26'', so the 0.2'' aperture contains almost only unique pixels. The corresponding masses are shown in Figure 7 assuming the dust temperature is equal to the source’s peak line brightness temperature (Section 3.4).

Except where noted below, the hand-selected sources are used for further analysis as they are more reliable.

### 3.4. Temperature estimation of the continuum sources

The temperature is a critical ingredient for determining the total mass of each continuum source or region. Since we do not have any means of directly determining the dust temperature, as the SED peak is well into the THz regime and

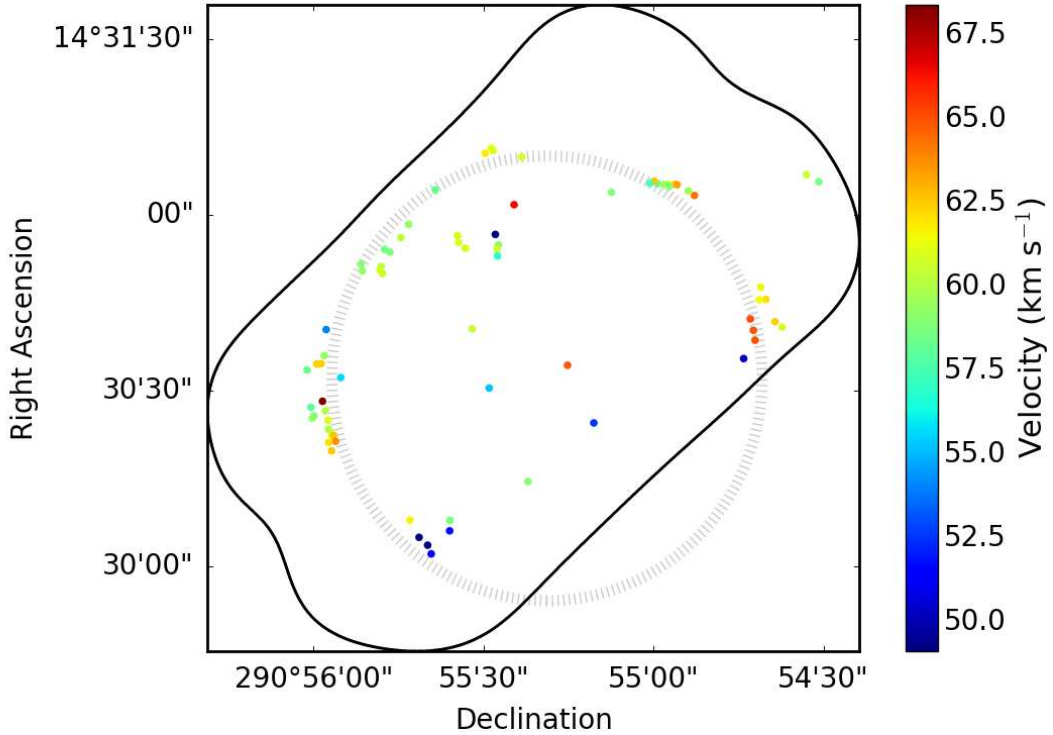


**Fig. 3.** The spatial distribution of the hand-identified core sample. The black outer contour shows the observed field of view. The dashed circle shows a hypothetical ring of star formation.

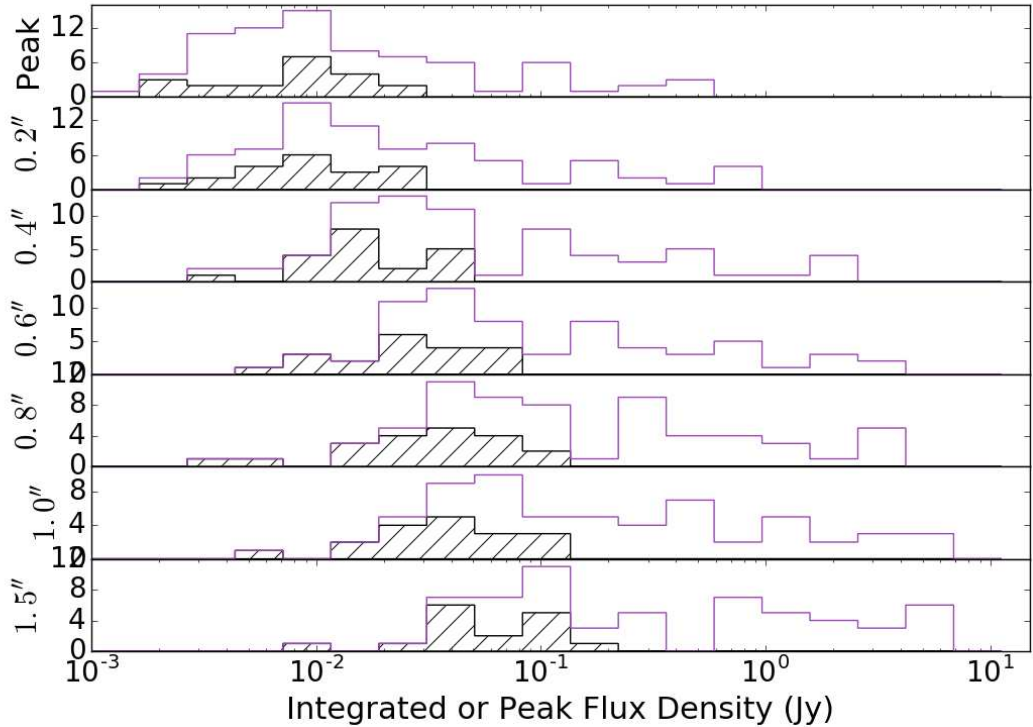


**Fig. 4.** Histograms of the core flux densities measured with circular apertures centered on the hand-extracted core positions. The aperture size is listed in the y-axis label. For the top plot, labeled ‘Peak’, this is the peak flux density in Jy/beam. For the rest, it is the integrated flux density in the specified aperture. The unfilled data show all sources and the hashed data are for starless core candidates (Section 3.5). See Figure 7 for the corresponding masses.

**Table 3.** Spectral Lines in SPW 1

| Line Name  | Frequency<br>GHz |
|--|------------------|
| H <sub>2</sub> CO 3 <sub>2,1</sub> – 2 <sub>2,0</sub>                      | 218.76007        |
| HC <sub>3</sub> N 24-23  | 218.32471        |
| HC <sub>3</sub> Nv <sub>7=1</sub> 24-23a                                   | 219.17358        |
| HC <sub>3</sub> Nv <sub>7=1</sub> 24-23a                                   | 218.86063        |
| HC <sub>3</sub> Nv <sub>7=2</sub> 24-23                                    | 219.67465        |
| OCS 18-17  | 218.90336        |
| SO 6 <sub>5</sub> – 5 <sub>4</sub>   | 219.94944        |
| HNCO 10 <sub>1,10</sub> – 9 <sub>1,9</sub>                                 | 218.98102        |
| HNCO 10 <sub>2,8</sub> – 9 <sub>2,7</sub>                                  | 219.73719        |
| HNCO 10 <sub>0,10</sub> – 9 <sub>0,9</sub>                                 | 219.79828        |
| HNCO 10 <sub>5,5</sub> – 9 <sub>5,4</sub>                                  | 219.39241        |
| HNCO 10 <sub>4,6</sub> – 9 <sub>4,5</sub>                                  | 219.54708        |
| HNCO 10 <sub>3,8</sub> – 9 <sub>3,7</sub>                                  | 219.65677        |
| CH <sub>3</sub> OH 8 <sub>0,8</sub> – 7 <sub>1,6</sub>                     | 220.07849        |
| CH <sub>3</sub> OH 25 <sub>3,22</sub> – 24 <sub>4,20</sub>                 | 219.98399        |
| CH <sub>3</sub> OH 23 <sub>5,19</sub> – 22 <sub>6,17</sub>                 | 219.99394        |
| C <sup>18</sup> O 2-1  | 219.56036        |
| H <sub>2</sub> CCO 11-10   | 220.17742        |
| HCOOH 4 <sub>3,1</sub> – 5 <sub>2,4</sub>                                  | 219.09858        |
| CH <sub>3</sub> OCHO 17 <sub>4,13</sub> – 16 <sub>4,12</sub> A             | 220.19027        |
| CH <sub>3</sub> CH <sub>2</sub> CN 24 <sub>2,22</sub> – 23 <sub>2,21</sub> | 219.50559        |
| Acetone 21 <sub>1,20</sub> – 20 <sub>2,19</sub> AE                         | 219.21993        |
| Acetone 21 <sub>1,20</sub> – 20 <sub>1,19</sub> EE                         | 219.24214        |
| Acetone 12 <sub>9,4</sub> – 11 <sub>8,3</sub> EE                           | 218.63385        |
| H <sub>2</sub> <sup>13</sup> CO 3 <sub>1,2</sub> – 2 <sub>1,1</sub>        | 219.90849        |
| SO <sub>2</sub> 22 <sub>7,15</sub> – 23 <sub>6,18</sub>                    | 219.27594        |
| SO <sub>2</sub> v <sub>2</sub> = 1 20 <sub>2,18</sub> – 19 <sub>3,17</sub> | 218.99583        |
| SO <sub>2</sub> v <sub>2</sub> = 1 22 <sub>2,20</sub> – 22 <sub>1,21</sub> | 219.46555        |
| SO <sub>2</sub> v <sub>2</sub> = 1 16 <sub>3,13</sub> – 16 <sub>2,14</sub> | 220.16524        |

**Table 4.** Spectral Lines in SPW 2

| Line Name  | Frequency<br>GHz |
|--|------------------|
| <sup>12</sup> CO 2 – 1   | 230.538          |
| OCS 19-18  | 231.06099        |
| HNCO 28 <sub>1,28</sub> – 29 <sub>0,29</sub>                                 | 231.873255       |
| CH <sub>3</sub> OH 10 <sub>2,9</sub> – 9 <sub>3,6</sub>                      | 231.28115        |
| <sup>13</sup> CS 5-4   | 231.22069        |
| NH <sub>2</sub> CHO 11 <sub>2,10</sub> – 10 <sub>2,9</sub>                   | 232.27363        |
| H30 $\alpha$   | 231.90093        |
| CH <sub>3</sub> OCHO 12 <sub>4,9</sub> – 11 <sub>3,8</sub> E                 | 231.01908        |
| CH <sub>3</sub> CH <sub>2</sub> OH 5 <sub>5,0</sub> – 5 <sub>4,1</sub>       | 231.02517        |
| CH <sub>3</sub> OCH <sub>3</sub> 13 <sub>0,13</sub> – 12 <sub>1,12</sub> AA  | 231.98772        |
| N <sub>2</sub> D+ 3-2  | 231.32183        |
| g-CH <sub>3</sub> CH <sub>2</sub> OH 13 <sub>2,11</sub> – 12 <sub>2,10</sub> | 230.67255        |
| g-CH <sub>3</sub> CH <sub>2</sub> OH 6 <sub>5,1</sub> – 5 <sub>4,1</sub>     | 230.79351        |
| g-CH <sub>3</sub> CH <sub>2</sub> OH 16 <sub>5,11</sub> – 16 <sub>4,12</sub> | 230.95379        |
| g-CH <sub>3</sub> CH <sub>2</sub> OH 14 <sub>0,14</sub> – 13 <sub>1,13</sub> | 230.99138        |
| SO <sub>2</sub> v <sub>2</sub> = 1 6 <sub>4,2</sub> – 7 <sub>3,5</sub>       | 232.21031        |
| CH <sub>3</sub> SH 16 <sub>2</sub> – 16 <sub>1</sub>                         | 231.75891        |
| CH <sub>3</sub> SH 7 <sub>3</sub> – 8 <sub>2</sub>                           | 230.64608        |

inaccessible with any existing instruments at the requisite resolution, we employ alternative indicators. Above a density  $n \gtrsim 10^5 - 10^6 \text{ cm}^{-3}$ , the gas and dust become strongly collisionally coupled, meaning the gas temperature should accurately reflect the dust temperature. Below this density, the two may be decoupled.

The average dust temperature, as estimated from Herschel Hi-Gal SED fits (Molinari et al. 2016; Wang et al. 2015), is 38 K when including the 70  $\mu\text{m}$  data or 26 K when excluding it. This average is obtained over a  $\sim 45''$  ( $\sim 1 \text{ pc}$ ) beam and therefore is likely to be strongly biased toward the hottest dust in the HII regions. Despite these

**Table 5.** Spectral Lines in SPW 3

| Line Name  | Frequency<br>GHz |
|--|------------------|
| CH <sub>3</sub> OH 4 <sub>2,3</sub> – 5 <sub>1,4</sub>               | 234.68345        |
| CH <sub>3</sub> OH 5 <sub>-4,2</sub> – 6 <sub>-4,3</sub>             | 234.69847        |
| CH <sub>3</sub> OH 18 <sub>3,15</sub> – 17 <sub>4,14</sub>           | 233.79575        |
| <sup>13</sup> CH <sub>3</sub> OH 5 <sub>1,5</sub> – 4 <sub>1,4</sub> | 234.01158        |
| PN 5 – 4   | 234.93569        |
| NH <sub>2</sub> CHO 11 <sub>5,6</sub> – 10 <sub>5,5</sub>            | 233.59451        |
| Acetone 12 <sub>11,2</sub> – 11 <sub>10,1</sub> AE                   | 234.86136        |
| SO <sub>2</sub> 16 <sub>6,10</sub> – 17 <sub>5,13</sub>              | 234.42159        |
| CH <sub>3</sub> NCO 27 <sub>2,26</sub> – 26 <sub>2,25</sub>          | 234.08812        |
| CH <sub>3</sub> SH 15 <sub>2</sub> – 15 <sub>1</sub>                 | 234.19145        |

**Table 6.** Continuum Source IDs and photometry Part 1

| Source ID | RA<br>°  | Dec<br>° | $S_{\nu}(0.2'')$ | $S_{\nu}(0.4'')$ | $T_{B,max}$<br>K | $M(T_{B,0.2''})$<br>$M_{\odot}$ | $M(T_{B,peak})$<br>$M_{\odot}$ | Categories |
|-----------|----------|----------|------------------|------------------|------------------|---------------------------------|--------------------------------|------------|
| ALMAmm1   | 290.9286 | 14.5022  |                  | 0.01             | 11               | 2.6                             | 2.6                            | fCc        |
| ALMAmm10  | 290.9114 | 14.5132  |                  | 0.01             | 5.3              | 2.6                             | 1                              | -Cc        |
| ALMAmm11  | 290.9112 | 14.5127  | 0.02             | 0.04             | 12               | 14                              | 12                             | -Cc        |
| ALMAmm12  | 290.9115 | 14.5127  | 0.01             | 0.02             | 11               | 3.7                             | 11                             | -C-        |
| ALMAmm13  | 290.9118 | 14.5112  | 0.01             | 0.01             | 11               | 5                               | 8.6                            | -Cc        |
| ALMAmm14  | 290.9107 | 14.5116  | 0.07             | 0.14             | 36               | 23                              | 23                             | -c         |
| ALMAmm15  | 290.9104 | 14.5114  | 0.01             | 0.03             | 35               | 4.9                             | 8.1                            | -c         |
| ALMAmm16  | 290.9092 | 14.5186  | 0.02             | 0.04             | 5.6              | 16                              | 32                             | -Cc        |
| ALMAmm17  | 290.9259 | 14.5151  | 0.01             | 0.03             | 12               | 11                              | 5                              | fCc        |
| ALMAmm18  | 290.9262 | 14.5154  | 0.01             | 0.03             | 5.6              | 11                              | 4.1                            | -Cc        |
| ALMAmm19  | 290.9263 | 14.5157  |                  | 0.01             | 21               | 3.2                             | 1.4                            | —          |
| ALMAmm2   | 290.9266 | 14.5022  |                  | 0.01             | 4                | 3                               | 12                             | fCc        |
| ALMAmm20  | 290.9235 | 14.5172  | 0.01             | 0.02             | 6.6              | 5.7                             | 4                              | -C-        |
| ALMAmm21  | 290.9249 | 14.5196  | 0.01             | 0.01             | nan              | 6.3                             | 31                             | -c         |
| ALMAmm22  | 290.9246 | 14.5198  | 0.01             | 0.02             | nan              | 6.1                             | 18                             | —          |
| ALMAmm23  | 290.9187 | 14.5178  | 0.02             | 0.07             | 26               | 11                              | 5.2                            | —          |
| ALMAmm24  | 290.9165 | 14.5182  | 0.29             | 0.6              | 72               | 46                              | 32                             | -Hc        |
| ALMAmm25  | 290.9255 | 14.5113  | 0.02             | 0.04             | 3.8              | 13                              | 6                              | fCc        |
| ALMAmm26  | 290.9296 | 14.5149  | 0.01             | 0.03             | 8.9              | 9.5                             | 14                             | -Cc        |
| ALMAmm27  | 290.9290 | 14.5156  | 0.01             | 0.03             | 5                | 7.2                             | 8.2                            | fC-        |
| ALMAmm28  | 290.9320 | 14.5090  | 0.02             | 0.03             | 19               | 11                              | 6.5                            | -Cc        |
| ALMAmm29  | 290.9247 | 14.5085  | 0.01             | 0.02             | nan              | 6.4                             | 11                             | f-c        |
| ALMAmm3   | 290.9267 | 14.5017  |                  | 0.01             | nan              | 3                               | 2.9                            | f-         |
| ALMAmm30  | 290.9298 | 14.5150  | 0.01             | 0.02             | 4.3              | 5.9                             | 2                              | fCc        |
| ALMAmm31  | 290.9156 | 14.5181  | 0.17             | 0.36             | 46               | 43                              | 16                             | -c         |
| ALMAmm32  | 290.9155 | 14.5181  | 0.09             | 0.23             | 94               | 1                               | 13                             | -H-        |
| ALMAmm33  | 290.9160 | 14.5181  | 0.19             | 0.51             | 48               | 48                              | 18                             | —          |
| ALMAmm34  | 290.9162 | 14.5181  | 0.08             | 0.24             | 9                | 1                               | 1                              | -H-        |
| ALMAmm35  | 290.9166 | 14.5183  | 0.2              | 0.58             | 34               | 76                              | 18                             | —          |
| ALMAmm36  | 290.9147 | 14.5176  | 0.02             | 0.05             | 11               | 16                              | 6.5                            | -Cc        |
| ALMAmm37  | 290.9243 | 14.5152  | 0.02             | 0.04             | 34               | 6.4                             | 3.1                            | -c         |
| ALMAmm38  | 290.9209 | 14.5095  |                  | 2                | 1.7              | 15                              | -Cc                            | —          |
| ALMAmm39  | 290.9245 | 14.5197  | 0.01             | 0.02             | 3.4              | 5.5                             | 25                             | -C-        |
| ALMAmm4   | 290.9276 | 14.5006  | 0.01             | 0.02             | 11               | 5.4                             | 6.1                            | -Cc        |
| ALMAmm40  | 290.9231 | 14.5194  | 0.01             | 0.02             | 9.2              | 5.3                             | 5.5                            | -Cc        |

uncertainties, this bulk measurement provides us with a reasonable range to assume for the uncoupled, low-density dust, which (weakly) dominates the mass (see Section 3.7).

One constraint on the dust temperature we can employ is the absolute surface brightness. For some regions, especially the e8 filament and the hot cores, the surface brightness is substantially brighter than is possible for a beam-filling, optically thick blackbody at 20 K, providing

a lower limit on the dust temperature ranging from 20 K (35 mJy/beam) to  $\sim$  300 K (0.5 Jy/beam). Toward most of this emission, optically-thick free-free emission can be strongly ruled out as the driving mechanism using existing data that limits the free-free contribution to be  $< 50\%$  if it is optically thick, and negligible ( $<< 1\%$ ) if it is optically thin at radio wavelengths (Ginsburg et al. 2016b; Goddi et al. 2016).

**Table 7.** Continuum Source IDs and photometry Part 2

| Source ID | RA<br>°  | Dec<br>° | $S_{\nu}(0.2'')$ | $S_{\nu}(0.4'')$ | $T_{B,max}$<br>K | $M(T_B, 0.2'')$<br>$M_{\odot}$ | $M(T_B, \text{peak})$<br>$M_{\odot}$ | Categories |
|-----------|----------|----------|------------------|------------------|------------------|--------------------------------|--------------------------------------|------------|
| ALMAmm41  | 290.9327 | 14.5112  | 0.02             | 0.03             | 3                | 8.6                            | 13                                   | -c         |
| ALMAmm43  | 290.9150 | 14.5178  | 0.02             | 0.05             | 17               | 14                             | 4.8                                  | fC-        |
| ALMAmm44  | 290.9086 | 14.5182  | 0.01             | 0.02             | 5.7              | 6                              | 28                                   | -Cc        |
| ALMAmm45  | 290.9115 | 14.5187  | 0.01             | 0.02             | 4.4              | 5.2                            | 1.8                                  | -C-        |
| ALMAmm46  | 290.9243 | 14.5147  | 0.01             | 0.04             | 24               | 8.5                            | 3                                    | —          |
| ALMAmm47  | 290.9274 | 14.5179  | 0.01             | 0.01             | 4.9              | 4.5                            | 9.2                                  | -Cc        |
| ALMAmm48  | 290.9287 | 14.5162  | 0.01             | 0.02             | 8.1              | 6.7                            | 13                                   | -Cc        |
| ALMAmm49  | 290.9300 | 14.5142  | 0.01             | 0.05             | 21               | 9.8                            | 7.6                                  | —          |
| ALMAmm5   | 290.9277 | 14.5010  | 0.01             | 0.02             | 5.9              | 7.3                            | 8.8                                  | -Cc        |
| ALMAmm50  | 290.9301 | 14.5141  | 0.02             | 0.05             | 14               | 14                             | 6.3                                  | -C-        |
| ALMAmm51  | 290.9300 | 14.5139  | 0.02             | 0.05             | 16               | 13                             | 2.7                                  | -C-        |
| ALMAmm52  | 290.9117 | 14.5107  |                  | 0.01             | 7.9              | 3.5                            | 1                                    | -Cc        |
| ALMAmm53  | 290.9119 | 14.5117  | 0.01             | 0.02             | 13               | 5.7                            | 5.6                                  | -Cc        |
| ALMAmm54  | 290.9122 | 14.5099  | 0.01             | 0.01             | 2.5              | 3.6                            | 9.7                                  | -Cc        |
| ALMAmm55  | 290.9309 | 14.5140  | 0.01             | 0.03             | 4.5              | 7.7                            | 6.5                                  | -C-        |
| ALMAmm56  | 290.9310 | 14.5143  | 0.01             | 0.03             | 5.3              | 6.4                            | 5.4                                  | -C-        |
| ALMAmm57  | 290.9239 | 14.5147  | 0.01             | 0.01             | 2                | 4                              | 1.2                                  | fCc        |
| ALMAmm6   | 290.9282 | 14.5014  |                  | 0.01             | 3.8              | 2                              | 1.1                                  | fC-        |
| ALMAmm7   | 290.9196 | 14.5068  |                  | 0.01             | 1.4              | 2.5                            | 7.1                                  | -Cc        |
| ALMAmm9   | 290.9228 | 14.5041  | 0.02             | 0.05             | 5.8              | 15                             | 9                                    | -Cc        |
| d2        | 290.9159 | 14.5180  | 0.16             | 0.43             | 99               | 18                             | 15                                   | -H-        |
| e1mm1     | 290.9327 | 14.5074  | 0.16             | 0.42             | 23               | 95                             | 31                                   | —          |
| e2e       | 290.9332 | 14.5096  | 0.69             | 1.9              | 84               | 94                             | 61                                   | -H-        |
| e2e peak  | 290.9332 | 14.5096  | 0.74             | 1.8              | 1                | 8                              | 68                                   | -Hc        |
| e2nw      | 290.9328 | 14.5100  | 0.22             | 0.51             | 4                | 69                             | 33                                   | -c         |
| e2se      | 290.9337 | 14.5093  | 0.04             | 0.1              | 93               | 4.4                            | 7.3                                  | -H-        |
| e2w       | 290.9330 | 14.5096  | 0.54             | 1.2              | 85               | 72                             | 6                                    | fHc        |
| e3mm1     | 290.9326 | 14.5069  | 0.05             | 0.18             | 23               | 29                             | 9.4                                  | —          |
| e5        | 290.9244 | 14.5157  | 0.03             | 0.03             | nan              | 18                             | 34                                   | F-c        |
| e8mm      | 290.9329 | 14.5078  | 0.68             | 1.7              | 18               | 43                             | 16                                   | -H-        |
| eEmm1     | 290.9334 | 14.5070  | 0.04             | 0.1              | 39               | 12                             | 7                                    | —          |
| eEmm2     | 290.9333 | 14.5071  | 0.04             | 0.1              | 22               | 24                             | 6.5                                  | —          |
| eEmm3     | 290.9335 | 14.5075  | 0.04             | 0.1              | 22               | 27                             | 8.1                                  | -c         |
| eSmm1     | 290.9326 | 14.5065  | 0.07             | 0.18             | 34               | 26                             | 2                                    | —          |
| eSmm2     | 290.9325 | 14.5062  | 0.07             | 0.17             | 29               | 31                             | 23                                   | -c         |
| eSmm2a    | 290.9323 | 14.5062  | 0.05             | 0.13             | 24               | 28                             | 18                                   | —          |
| eSmm3     | 290.9323 | 14.5059  | 0.05             | 0.1              | 29               | 23                             | 16                                   | -c         |
| eSmm4     | 290.9326 | 14.5059  | 0.04             | 0.1              | 27               | 17                             | 1                                    | —          |
| eSmm6     | 290.9325 | 14.5055  | 0.05             | 0.11             | 23               | 29                             | 15                                   | -c         |
| north     | 290.9169 | 14.5182  | 0.72             | 1.7              | 69               | 12                             | 59                                   | -Hc        |

The Categories column consists of three letter codes as described in Section 3.5. In column 1, F indicates a free-free dominated source, f indicates significant free-free contribution, and - means there is no detected cm continuum. In column 2, the peak brightness temperature is used to classify the temperature category. H is ‘hot’ ( $T > 50$  K), C is ‘cold’ ( $T < 20$  K), and - is indeterminate (either  $20 < T < 50$  K or no measurement). In column 3, c indicates compact sources, and - indicates a diffuse source.

To gain a more detailed measurement of the dust temperature in regions where it is likely to be coupled to the gas, we use the peak brightness temperature  $T_{B,max}$  of spectral lines along the line of sight. If the observed molecule is in local thermal equilibrium, as is expected if the density is high enough to be collisionally coupled to the dust, and it is optically thick, the brightness temperature provides an approximate measurement of the local temperature near the  $\tau = 1$  surface. If any of these assumptions do not hold,  $T_{B,max}$  will set a lower limit on the true gas temperature. Only two mechanisms can push  $T_{B,max} > T_{dust}$ : nonthermal (maser) emission or a dust-emitting region that has a smaller beam filling factor than the gas-emitting region.

One potential problem with this approach is if the gas becomes optically thick before probing most of the dust. Some transitions of more abundant molecules, e.g., CO and H<sub>2</sub>CO, are likely to be affected by this issue. However, many of the molecules included in the observations have lower abundances and are likely to be optically thin along most of the line of sight.

Some sources have no detected line emission aside from the molecular cloud species CO and H<sub>2</sub>CO. The minimum density requirement imposed by a continuum detection at our limit of 1.6 mJy is  $n > 10^{7.5} \text{ cm}^{-3}$  for a spherical source. At such high density, it is unlikely that the species are undetected because they are subthermally excited. More likely,

the line-nondetection sources have an underlying emission source that is very compact, optically thick, and/or cold.

Figure 5 shows the distribution of peak line brightnesses for the continuum sources. The spectra used to determine this brightness are the spectra obtained from the brightest continuum pixel within the source aperture. To obtain the peak line brightness, we fit Gaussian profiles to each identified line listed in Tables 2–5, rejecting those with poor fits. The line brightnesses reported in the figure are the sum of the continuum-subtracted peak line brightness and the continuum brightness (i.e., they are the raw observed peak brightness). Excepting CO and H<sub>2</sub>CO, which are excluded from the plot, CH<sub>3</sub>OH is the brightest line toward most sources.

We use these peak line brightness temperatures to compute the ‘corrected’ masses of the continuum sources. For sources with  $T_{B,max} < 20$  K, we assume  $T_{dust} = 20$  K to avoid producing unreasonably high masses; in such sources the lines are likely to be optically thin and/or subthermally excited. The correction is illustrated in Figure 6.

This section has provided some simple temperature estimates across all of the detected continuum sources. In Section 3.9, we will examine the thermal structure of the hot cores in more detail.

### 3.5. The nature of the continuum sources

Millimeter continuum sources in star-forming regions are usually assumed to be either protostars or starless cores. However, in this high-mass star-forming region, we have to consider both those possibilities and potential free-free sources or high-luminosity main-sequence stars embedded in dust.

We fit each of up to  $\sim 50$  lines (see Tables 2–5) with Gaussian profiles to attempt to determine the relative line strengths toward each source. Most sources were detected in at least  $\sim 5 - 10$  lines, though some of these are associated with interstellar rather than circumstellar material, i.e., H<sub>2</sub>CO, CO, <sup>13</sup>CS. For sources with detections in non-interstellar lines, we used the peak brightness temperature of the line as an estimated lower limit on the core temperature.

In the continuum, we measured a ‘concentration parameter’, which is the ratio of the flux density in a  $0.2''$  aperture to that in a  $0.2''$ – $0.4''$  annulus divided by three to account for the annulus’ larger area. A uniform source with  $r > 0.4''$  source would have a concentration  $C = 1$  by this definition, while an unresolved point source would have a Gaussian profile resulting in  $C = 14$ . Only one source approaches this extreme, the HII region e5, while the rest have  $C \leq 7$ . We set the threshold for a ‘concentrated’ source to be  $C > 2$ , which is arbitrary, but does a reasonable job of distinguishing the sources with a clear central concentration from those that have none.

Main sequence OB stars and their illuminated ionized nebulae are in principle easily identified by their free-free emission. Starless cores, protostellar cores, and their variants are more difficult to identify, so we used a combination of temperature and concentration parameter to classify them.

We classified each of the 75 hand-selected sources on the following parameters:

1. Free-free dominated sources ( $S_{15GHz} > 0.5S_{226GHz}$ ) are H II regions
2. Free-free contaminated sources ( $S_{15GHz} > 0.1S_{226GHz}$ ) are likely to be dust-dominated but with H II region contamination; these are either dusty sources superposed on or embedded in a large H II region or they are compact, dusty H II regions
3. Starless core candidates were identified as those with cold peak brightness temperatures  $T_B < 20$  K and with a high concentration parameter ( $C > 2$ )
4. Hot core candidates are those with peak  $T_B > 50$  K and  $C > 2$
5. Extended cold core and hot core candidates are those with  $T_B < 20$  and  $T_B > 50$  K and  $C < 2$
6. The remaining sources with  $S_{15GHz} < 0.1S_{226GHz}$  and  $50 > T_B > 20$  K were classed as uncertain compact ( $C > 2$ ) or uncertain extended ( $C < 2$ )

These classifications are set in the ‘Categories’ column of Table 7. They serve as a broad guideline for further analysis.

#### 3.5.1. W51e2e mass and temperature estimates from continuum

In a  $0.21'' \times 0.19''$  beam ( $1100 \times 1000$  au), the peak flux density toward W51 e2e is 0.38 Jy, which corresponds to a brightness temperature  $T_B = 225$  K. This is a lower limit to the surface brightness of the millimeter core, since an optical depth  $\tau < 1$  or a filling factor of the emission  $ff < 1$  would both imply higher intrinsic temperatures. The implied luminosity, assuming blackbody emission from a spherical beam-filling source, is  $L = 4\pi r^2 \sigma_{sb} T^4 = 2.3 \times 10^4 L_\odot$ . Since any systematic uncertainties imply a higher temperature, this estimate is a lower limit on the source luminosity.

If we assume that the dust is optically thick throughout our beam, and assume an opacity constant  $\kappa(226GHz) = 120 \text{ g cm}^{-2}$ , the minimum mass per beam to achieve  $\tau \geq 1$  is  $M = 18 M_\odot \text{ beam}^{-1}$ . This mass is not a strict limit in either direction: if the dust is indeed optically thick, there may be substantial hidden or undetected gas, while if the filling factor is lower than 1, the dust may be much hotter and therefore optically thin and lower mass. However, simulations and models both predict that the dust will become highly optically thick at radii  $r \lesssim 1000$  au (Forgan et al. 2016; Klassen et al. 2016), so it is likely that this measurement provides a lower limit on the total gas mass surrounding the protostar.

For an independent measurement of the temperature that is not limited to the optically thick regions, we use the CH<sub>3</sub>OH lines in band, calculating an LTE temperature that is  $200 < T < 600$  K out to  $r < 2''$  ( $r < 10^4$  au; Section 3.9). As noted in Section 3.9, these temperatures may be overestimates when the low-J lines of CH<sub>3</sub>OH are optically thick, but for now they are the best measurements we have available. If the dust temperature matches the methanol temperature, it would be optically thin ( $\tau \lesssim 1/3$ ) and the mass would be only  $\sim 6 M_\odot$ . However, this latter estimate discounts any substructure at scales  $< 1000$  AU, which we know exists from the 2015.1.01596.S data.

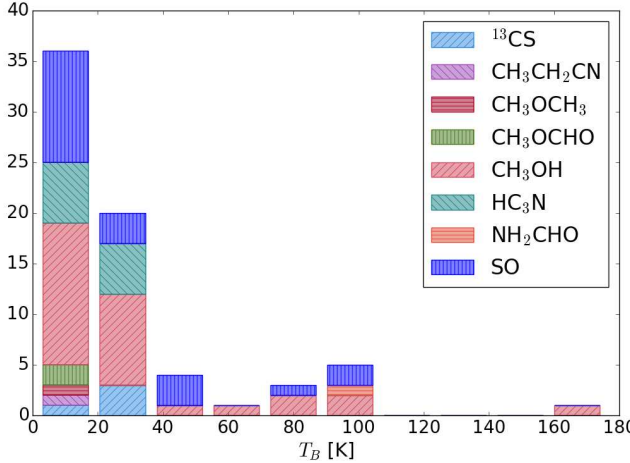


**Fig. 5.** Histogram of the brightest line toward each continuum source. The bars are colored by the molecular species associated with the brightest line that is not associated with extended molecular cloud emission, i.e., CO and its isotopologues and H<sub>2</sub>CO are excluded.

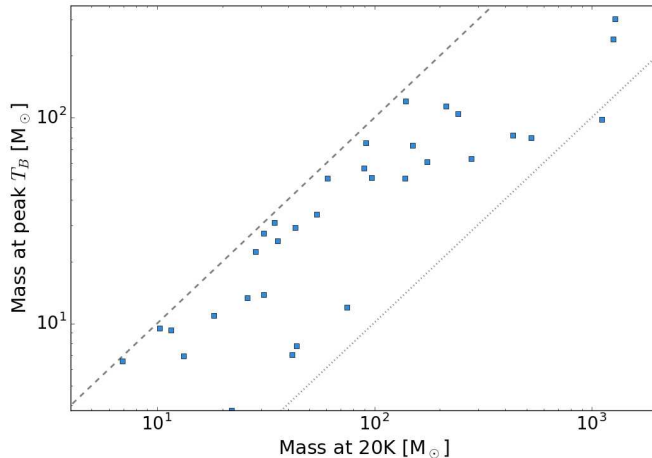


**Fig. 6.** The mass computed assuming the dust temperature is the peak brightness temperature vs. that computed assuming  $T_{dust} = 20$  K for the aperture extracted continuum sources. The dashed line shows  $M(T_{B,max}) = M(20\text{K})$  and the dashed line shows  $M(T_{B,max}) = 0.1M(20\text{K})$

### 3.5.2. W51 e8 and north mass and temperature from continuum

We repeat the above analysis for e8 and north. They have peak flux densities of 0.35 and 0.44 Jy/beam respectively, corresponding to peak brightness temperatures of 205 and 256 K. The lower limit luminosities of W51 e8 and north in a single beam, assuming the brightest detected beam is optically thick, are  $1.6 \times 10^4$  and  $3.9 \times 10^4 L_\odot$ , respectively.

### 3.6. Radial mass profiles around the most massive cores

In Figure 8, we show the radial profiles extracted from the three high-mass protostellar cores in W51: W51 North, W51 e2e, and W51 e8. The plot shows the enclosed mass out to  $\sim 1''$  (5400 AU). On larger spatial scales, the enclosed mass rises more shallowly, indicating the end of the core.

All three sources show similar radial profiles, containing up to  $3000 M_\odot$  within a compact radius of 5400 AU (0.03 pc). However, the temperature structure within these

sources is certainly not homogeneous, and likely a large fraction of the total flux comes from  $T \gtrsim 300$  K heated material (Section 3.4; Goddi et al. 2016). If the observed dust were all at 600 K, the mass would be  $\sim 17 \times$  lower,  $100 M_\odot$ , which we treat as a strict lower bound as it is unlikely that the dust at more than  $r \gtrsim 1000$  AU is so warm. Additionally, it is likely that a substantial mass of cold dust is also present but undetectable because it is hidden by the hotter dust.

### 3.7. The mass and light budget on different spatial scales

An evolutionary indicator used for star-forming regions is the amount of mass at a given density; a more evolved (more efficiently star-forming) region will have more mass at high densities. We cannot measure the dense gas fraction directly, but the amount of flux density recovered by an interferometer provides an approximation.

For the “total” flux density in the region, we use the Bolocam Galactic Plane Survey observations (Aguirre et al.

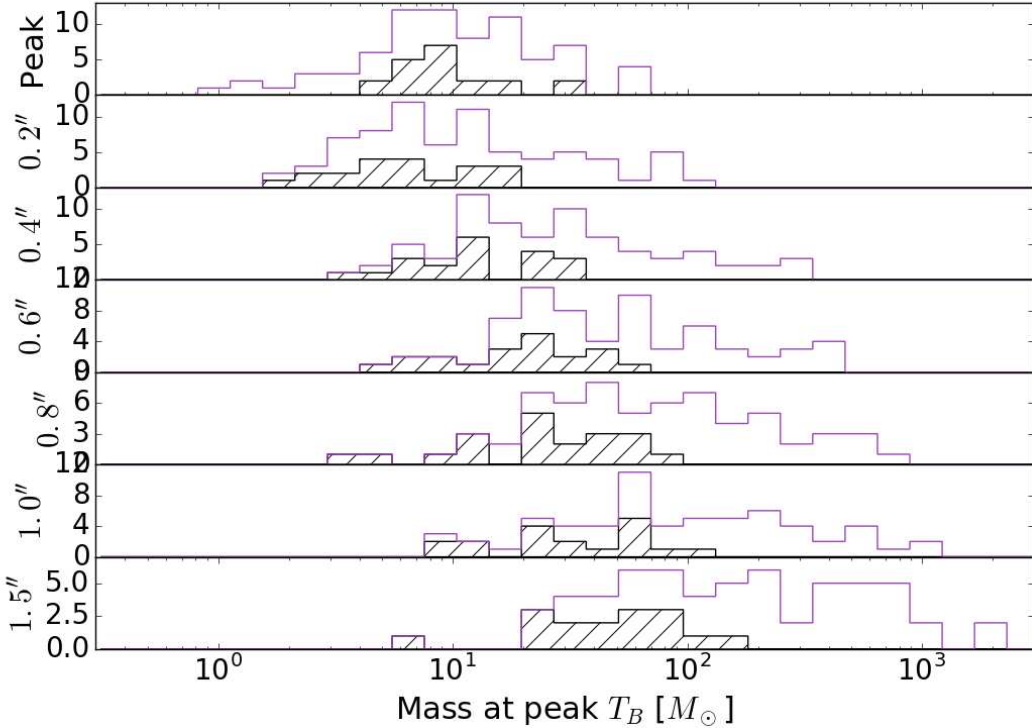


**Fig. 7.** Histograms of the core masses computed from the flux density measurements shown in Figure 4 using the peak brightness temperature toward the center of that source as the dust temperature. The aperture size is listed in the y-axis label. For the top plot, labeled ‘Peak’, the mass is computed from peak flux density in Jy/beam. For the rest, it is the integrated flux density in the specified aperture in Jy. The unfilled data show all sources and the hashed data are for starless core candidates (Section 3.5).

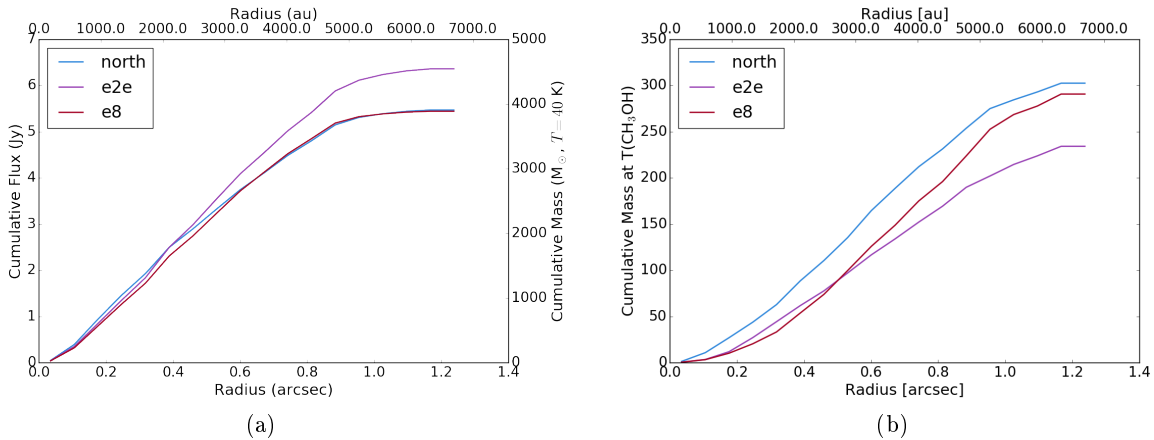


**Fig. 8.** The cumulative flux density radial profiles centered on three massive protostellar cores. They share similar profiles and are likely dominated by hot dust in their innermost regions, but they are more likely to be dominated by cooler dust in their outer, more massive regions. The cumulative mass distribution may therefore be deceptive. In (a), we use a constant temperature. In (b), we use the temperature map computed from  $\text{CH}_3\text{OH}$  in Section 3.9.

2011; Ginsburg et al. 2013), which are the closest in frequency single-dish millimeter data available. We assume a spectral index  $\alpha = 3.5$  to convert the BGPS flux density measurements at 271.4 GHz to the mean ALMA frequency of 226.6 GHz. The ALMA data (specifically, the 0.2'' resolution 12m-only data) have a total flux 23.2 Jy above a conservative threshold of 10 mJy/beam in our mosaic; in the same area the BGPS data have a flux of 144 Jy, which scales down to 76.5 Jy. The recovery fraction is  $30 \pm 3\%$ ,

where the error bar accounts for a change in  $\alpha \pm 0.5$ . The threshold of 10 mJy/beam corresponds to a column threshold  $N > 1.3 \times 10^{25} \text{ cm}^{-3}$  for 20 K dust. This threshold also corresponds to an optical depth of  $\tau \approx 0.5$ , implying that a large fraction of the cloud is either approaching optically thick or warmer than 20 K. For an unresolved spherical source in the  $\sim 0.2''$  beam, this column density corresponds to a volume density  $n > 10^{8.1} \text{ cm}^{-3}$ .

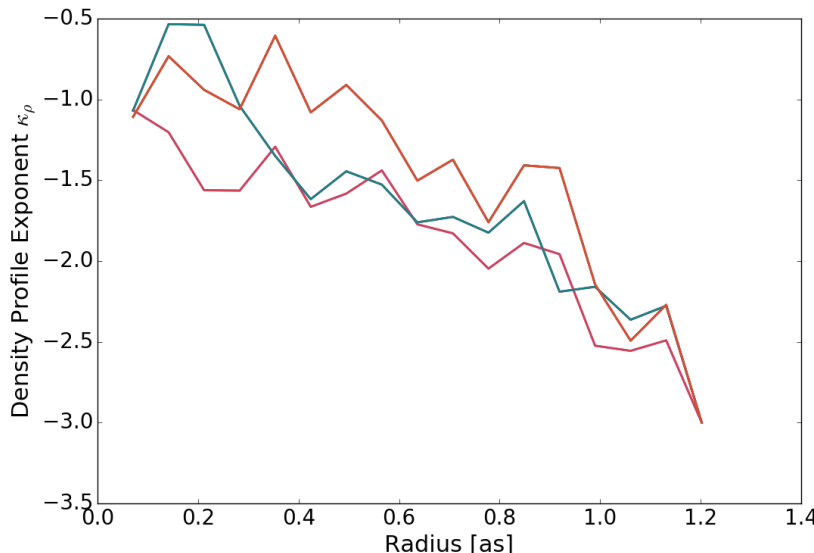


**Fig. 9.** This figure is meant for discussion, not necessarily final publication. The radial mass profile exponent  $\kappa_\rho$  as a function of radius. The ‘fiducial value’ used in the McKee/Tan model is  $\kappa_\rho = -1.5$  (where I’ve flipped the sign...), but importantly it is *constant* at  $t = 0$ . What are the consequences of a non-constant  $\kappa_\rho$ ?

Even more impressive is the amount of the total flux density concentrated into the three ‘massive cores’, W51 e2e, e8, and north. These three contain 12.3 Jy (within 1'' or 5400 AU apertures) of the total 23.2 Jy in the observed field - more than half of the total ALMA flux density, or 15% of the BGPS flux density. In a Kroupa (2001) IMF, massive stars ( $M > 20 M_\odot$ ) account for only 0.15% of the mass, so in order for the gas mass distribution to produce a ‘normal’ stellar distribution, the high-mass-star-producing gas must be much brighter (hotter) than that making low-mass stars, or the gas must be substantially redistributed and fragmented as the region evolves.

### 3.8. Chemically Distinct Regions

The “hot cores” in W51 (e2, e8, and North) are spatially well-resolved and multi-layered. These cores are detected in lines of many different species spanning areas  $\sim 5 \times 10^3 - 10^4$  AU across.

Surrounding W51e2e, there are relatively sharp-edged uniform-brightness regions in a few spectral lines over the range 51-60 km s $^{-1}$  (Figure 10). Some of these features are elongated in the direction of the outflow, but most have significant extent orthogonal to the outflow, spanning  $9500 \times 6600$  AU. They are prominent in CH<sub>3</sub>OH, OCS, and CH<sub>3</sub>OCH<sub>3</sub>, weak but present in H<sub>2</sub>CO and SO, and absent in HC<sub>3</sub>N and HNCO.

Around e8, a similar feature is observed, but in this case CH<sub>3</sub>OCH<sub>3</sub> is absent. Toward W51 north, CH<sub>3</sub>OH, H<sub>2</sub>CO, and SO exhibit the sharp-edged enhancement feature, while the other species do not. The enhancement is from 50-60 km s $^{-1}$ .

By contrast, along the south end of the e8 filament, no such enhanced features are seen; only H<sub>2</sub>CO and the lowest transition of CH<sub>3</sub>OH are evident.

The relative chemical structures of e2, e8, and IRS2 are similar. The same species are detected in all of the central cores. However, in e2, CH<sub>3</sub>OCH<sub>3</sub>, CH<sub>3</sub>OCHO, CH<sub>3</sub>CH<sub>2</sub>CN,

and Acetone ([CH<sub>3</sub>]<sub>2</sub>CO) are significantly more extended than in the other sources. g-CH<sub>3</sub>CH<sub>2</sub>OH is detected in W51 North, but is weak in e8 and almost absent in e2 (Figures 10, 11, 12, 13).

Different chemical groups exhibit different morphologies around e2. Species that are elongated in the NW/SE direction are associated primarily with the outflow (HC<sub>3</sub>N, CH<sub>3</sub>CH<sub>2</sub>CN). Other species are associated primarily with the extended core (CH<sub>3</sub>OCHO, CH<sub>3</sub>OCH<sub>3</sub>, [CH<sub>3</sub>]<sub>2</sub>CO). Some are only seen in the compact core (H<sub>2</sub>CN, HNCO, NH<sub>2</sub>CHO, and vibrationally excited HC<sub>3</sub>N). Only CH<sub>3</sub>OH and OCS are associated with both the extended core and the outflow, but not the greater extended emission. H<sub>2</sub>CCO seems to be associated with only the extended core, but not the compact core. Finally, there are the species that trace the broader ISM in addition to the cores and outflows (H<sub>2</sub>CO, <sup>13</sup>CS, OCS, C<sup>18</sup>O and SO). Both HCOOH and N<sub>2</sub>D $^+$  are weak and associated only with the innermost e2e core.

The presence of these complex species symmetrically distributed at large distances ( $r \sim 5000$  AU) from the central sources is an independent indication of the gas heating provided by these sources.

### 3.9. CH<sub>3</sub>OH temperatures & columns in the hot cores

The chemically enhanced regions appear to be associated with regions of elevated gas temperature. We examine this directly by analyzing the excitation of lines for which we have detected multiple transitions with significant energy differences. We do not use H<sub>2</sub>CO for this analysis despite its usefulness as a thermometer because it is clearly optically thick (self-absorbed) in all lines in the hot cores.

We produce rotational diagrams for each spatial pixel covering all CH<sub>3</sub>OH lines detected at high significance toward at least one position. The detected lines span a range  $45 < E_U < 800$  K, allowing robust measurements of the temperature assuming the lines are optically thin, in LTE,

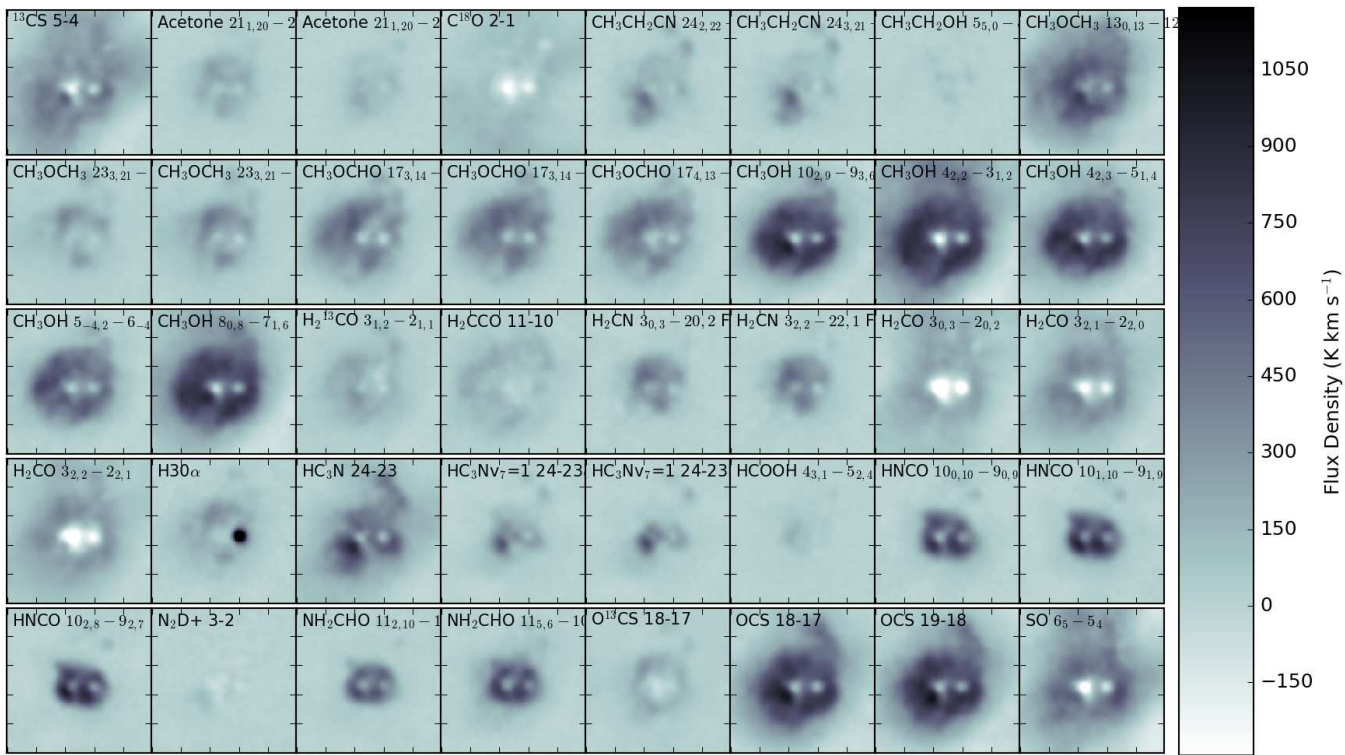


**Fig. 10.** Moment 0 maps of the e2 region in 40 different lines over the range 51 to 60 km s<sup>-1</sup> with continuum subtraction using the 30th percentile emission over the ranges 25-40 and 75-90 km s<sup>-1</sup>. All images are on the same scale, and the negative features show absorption against the continuum. There is a strong ‘halo’ of emission seen in the CH<sub>3</sub>Ox lines and OCS. Extended emission is also clearly seen in SO, <sup>13</sup>CS, and H<sub>2</sub>CO, though these lines more smoothly blend into their surroundings. HNCO and NH<sub>2</sub>CHO have smaller but substantial regions of enhancement with a sharp contrast to their surroundings. HC<sub>3</sub>N traces the e2 outflow. The bright H30 $\alpha$  emission marks the position of e2w, the hypercompact HII region that dominates the centimeter emission in e2.

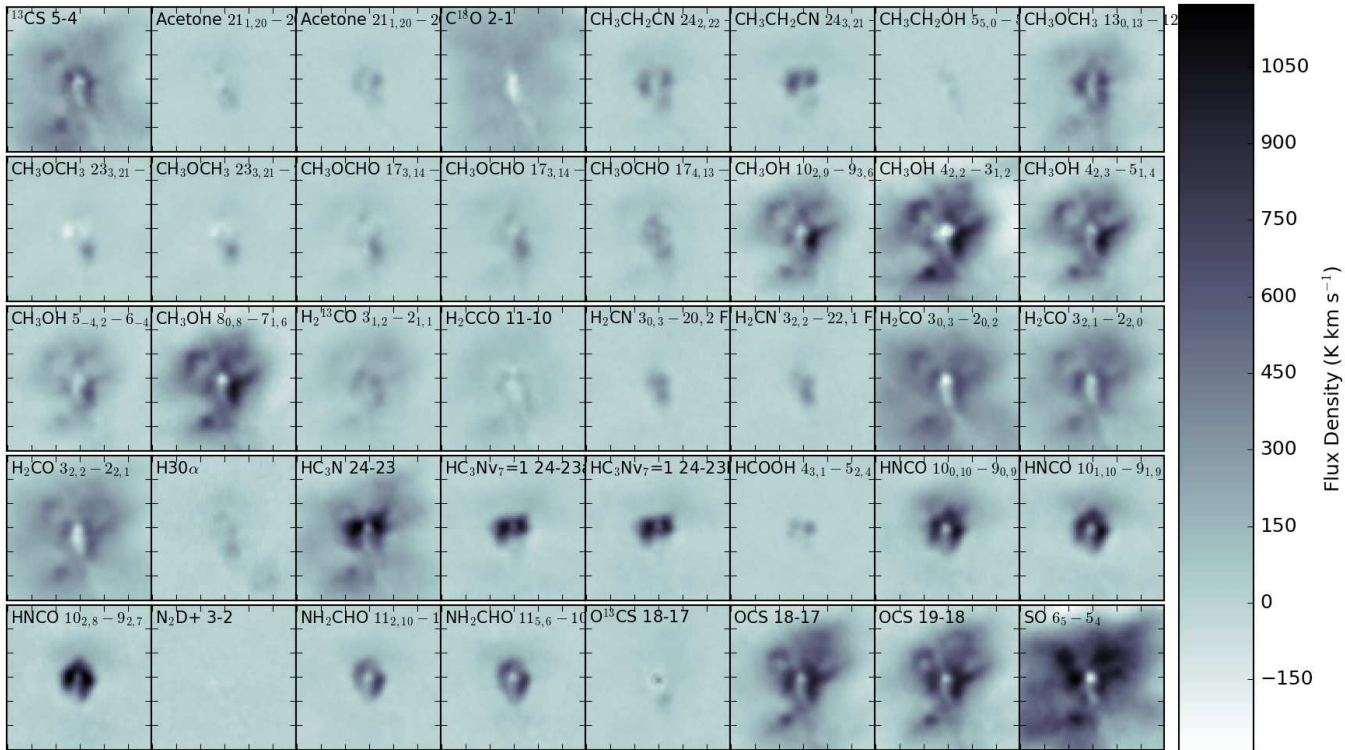


**Fig. 11.** Moment 0 maps of the e8 region in 40 different lines over the range 52 to 63 km s<sup>-1</sup> with continuum subtraction using the 30th percentile emission over the ranges 25-40 and 75-90 km s<sup>-1</sup>. All images are on the same scale, and the negative features show absorption against the continuum. As in e2, there is extended emission in the CH<sub>3</sub>OH and OCS lines, but in contrast with e2, the other CH<sub>3</sub>Ox lines are more compact. SO is brighter than OCS in e8, whereas the opposite is true in e2.

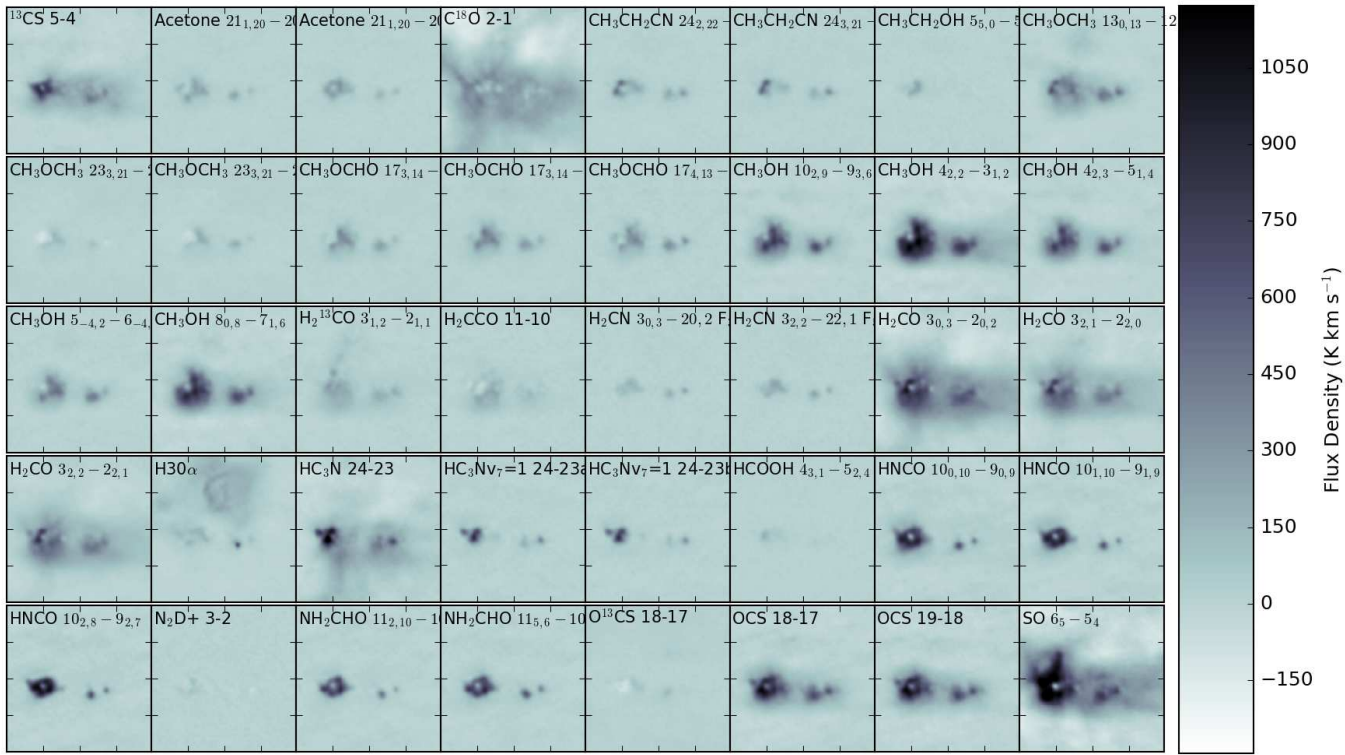


**Fig. 12.** Moment 0 maps of the W51 IRS2 region in 40 different lines over the range 54 to 64  $\text{km s}^{-1}$  with continuum subtraction using the 30th percentile emission over the ranges 25-40 and 75-90  $\text{km s}^{-1}$ . All images are on the same scale, and the negative features show absorption against the continuum. Qualitatively, the relative extents of species seem comparable to e8. The H30 $\alpha$  point source is W51 d2.

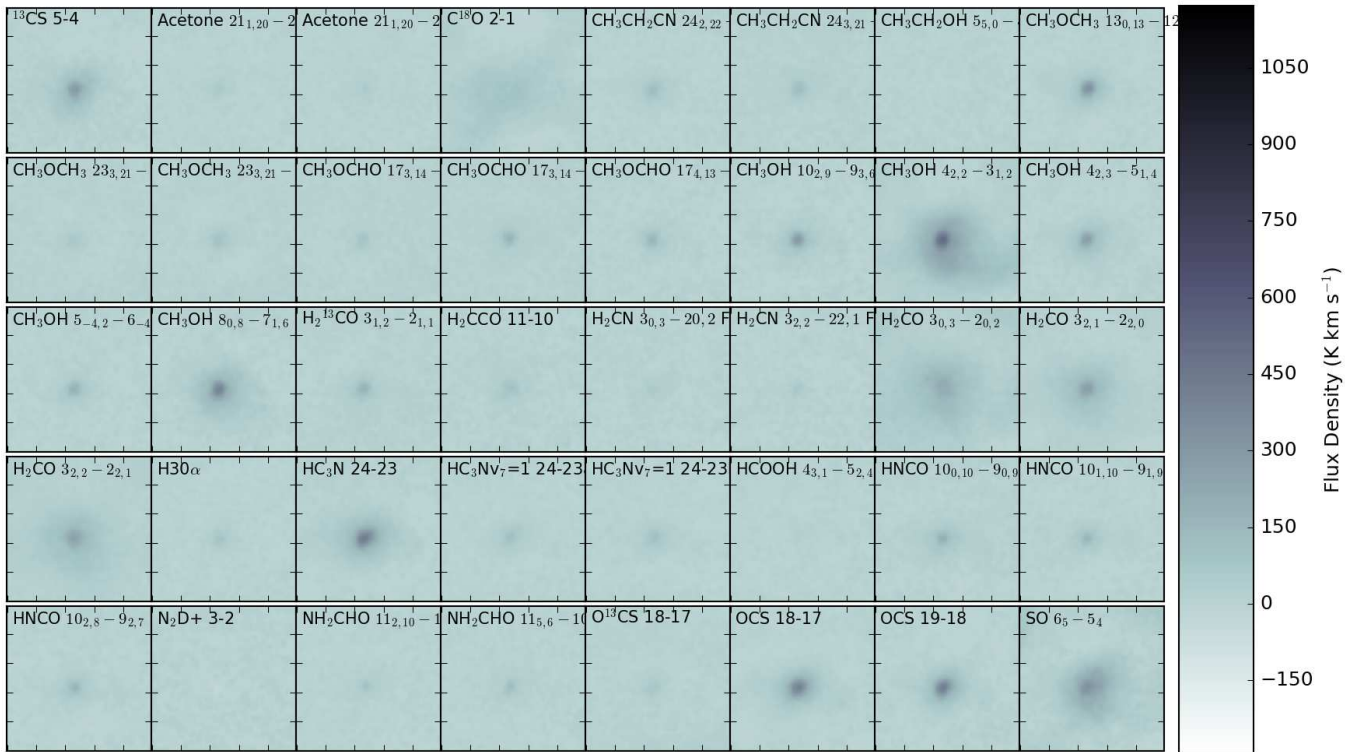


**Fig. 13.** Moment 0 maps of the ALMAmm14 region in 40 different lines over the range 58 to 67  $\text{km s}^{-1}$  with continuum subtraction using the 30th percentile emission over the ranges 25-40 and 75-90  $\text{km s}^{-1}$ . All images are on the same scale. ALMAmm14 is one of the brightest sources outside of e2/e8/IRS2, but it is substantially fainter than those regions. Still, it has a noticeably rich chemistry.

and the gas temperature is high enough to excite the lines. These conditions are likely to be satisfied in the e2e, e8, and North cores, except for the optically thin requirement. Luckily, there are some lines in band that have much lower Einstein  $A_{i,j}$  values but comparable upper-state energy levels, allowing us to probe higher column densities than would otherwise be possible.

Sample fitted rotational diagrams are displayed in Figure 15. The line intensities are computed from moment maps integrating over the range  $(51, 60) \text{ km s}^{-1}$  in continuum-subtracted spectral cubes, where the continuum was estimated as the median over the ranges  $(25\text{--}35, 85\text{--}95) \text{ km s}^{-1}$ , except for the  $J=25$  lines, which had a continuum estimated from the 10th percentile over the same range to exclude contamination from the SO outflow line wings.

To validate some of the rotational diagram fits, we examined the modeled spectra overlaid on the real (Figure 16). These generally display significant discrepancies, especially at low  $J$  where self-absorption is evident. In Figure 16, there is clearly a low-temperature component slightly redshifted from the high- $J$  peak that can be seen as a dip within the line profile. The presence of this unmodeled low-temperature component renders our  $\text{CH}_3\text{OH}$  temperature measurements uncertain. Nevertheless, the general trend exhibited by  $\text{CH}_3\text{OH}$  temperatures matches expectations if there is a central heating source.

Figure 17 shows a comparison between the  $\text{CH}_3\text{OH}$   $10_{2,9} - 9_{3,6}$  line and the 225 GHz continuum. While the brightest regions in  $\text{CH}_3\text{OH}$  mostly have corresponding dust emission, the dust morphology traces the  $\text{CH}_3\text{OH}$  morphology very poorly. This difference suggests that the enhanced brightness is not simply because of higher total column density. We examine the dust- $\text{CH}_3\text{OH}$  link more quantitatively in Figure 19.

Figure 18 shows the observed brightness profiles of  $\text{CH}_3\text{OH}$  line and dust continuum emission. Figure 19 shows a comparison of the  $\text{CH}_3\text{OH}$  temperature and abundance. The  $\text{CH}_3\text{OH}$  abundance is derived by comparing the rotational diagram (RTD) fitted  $\text{CH}_3\text{OH}$  column density to the dust column density while using the  $\text{CH}_3\text{OH}$ -derived temperature as the assumed dust temperature. The figure shows all pixels within a  $3''$  (16200 AU) radius of e2e, with pixels having low column density and high temperature (i.e., pixels with bad fits) and those near e2w (which may be heated by a different source) excluded. We used moment-0 (integrated intensity) maps of the  $\text{CH}_3\text{OH}$  lines to perform these RTD fits, which means we have ignored the line profile entirely and in some cases underestimated the intensity of the optically thick lower- $J$  lines: in the regions of highest column, the column is underestimated and the temperature is overestimated, as can be seen in Figure 16.

A few features illustrate the effects of thermal radiative feedback on the gas. The temperature jump starting inwards of  $r \sim 1.5''$  (8100 AU; Figure 19b) is substantial, though the 100-200 K floor at greater radii is likely artificial as the low- $J$  transitions are not consistent with a thermal distribution. There is an abundance enhancement at the inner radii, but it appears to be a radial bump rather than a pure increase. The abundance enhancement is probably real, and is approximately a factor of  $\sim 5 - 10$ . The inner abundance dip is caused by two coincident effects: first, the  $\text{CH}_3\text{OH}$  column becomes underestimated because the  $\text{CH}_3\text{OH}$  is *self*-absorbed, and second, the dust becomes op-

tically thick, blocking additional  $\text{CH}_3\text{OH}$  emission, though this latter effect is somewhat self-regulating since it also decreases the dust column (the denominator in the abundance expression).

### 3.10. Ionizing vs non-ionizing radiation

The formed and forming protostars are producing a total  $\gtrsim 10^7 L_\odot$  of far infrared illumination (Ginsburg et al. 2016b). This radiation heats the cloud's molecular gas, affecting the initial conditions of future star formation.

The ionizing radiation in W51 was discussed in detail in (Ginsburg et al. 2016b). Ionizing radiation affects much of the cloud, but little of the high-density prestellar material. There is no evidence of increased gas temperatures in the vicinity of HII regions. While in Section 3.8 we identify chemically enhanced regions as those where radiative feedback has heated the dust and released ices into the gas phase, no such regions are observed surrounding the most luminous compact HII regions.

The chemical maps shown in Section 3.8 show the volumes of gas clearly affected by newly-forming high-luminosity stars. The  $\text{CH}_3\text{OH}$ -enhanced region around W51e2 extends 0.04 pc, or 8500 AU (see Section 3.9). Other locally enhanced species, especially the nitrogenic molecules HNCO and  $\text{NH}_2\text{CHO}$ , occupy a smaller and more asymmetric region around e2e and e2w (Figure 20). These chemically enhanced regions are most prominent around the weakest radio sources or regions with no radio detection; they are most likely heated by direct infrared radiation from these sources.

### 3.11. Outflows

We detected many outflows, primarily in CO 2-1 and SO  $6_5 - 5_4$ . The flows are weakly detected in some other lines, e.g.  $\text{H}_2\text{CO}$ , but we defer discussion of outflow chemistry to a future work.

In this section, we discuss some of the unique outflows and unique features of outflows in the W51 region. We show the most readily identified outflows in Figures 24, 23, 25, and 26.

#### 3.11.1. The Lacy jet

A high-velocity outflow was discovered within the W51 IRS2 region by Lacy et al. (2007), and subsequently detected in H77 $\alpha$  by Ginsburg et al. (2016b). We have discovered the CO counterpart to this outflow, which comes from near the continuum source ALMAMm31 (Figure 22). Strangely, though, the outflow is not directly centered on the millimeter continuum source, but is slightly offset. The outflow shows red- and blue-shifted lobes that form the base of the ionized outflow reported by Lacy et al. (2007, Figure 23).

The presence of the Lacy jet is important for ruling out outflows from HII regions. It provides clear evidence that a molecular outflow that is subsequently ionized can be easily detected in existing radio recombination line data. If outflows of comparable mass were being launched from the stars at the centers of HCHII regions (e.g., e2w), we would detect these flows. Their absence provides an upper limit on the outflow rate - and presumably the accretion

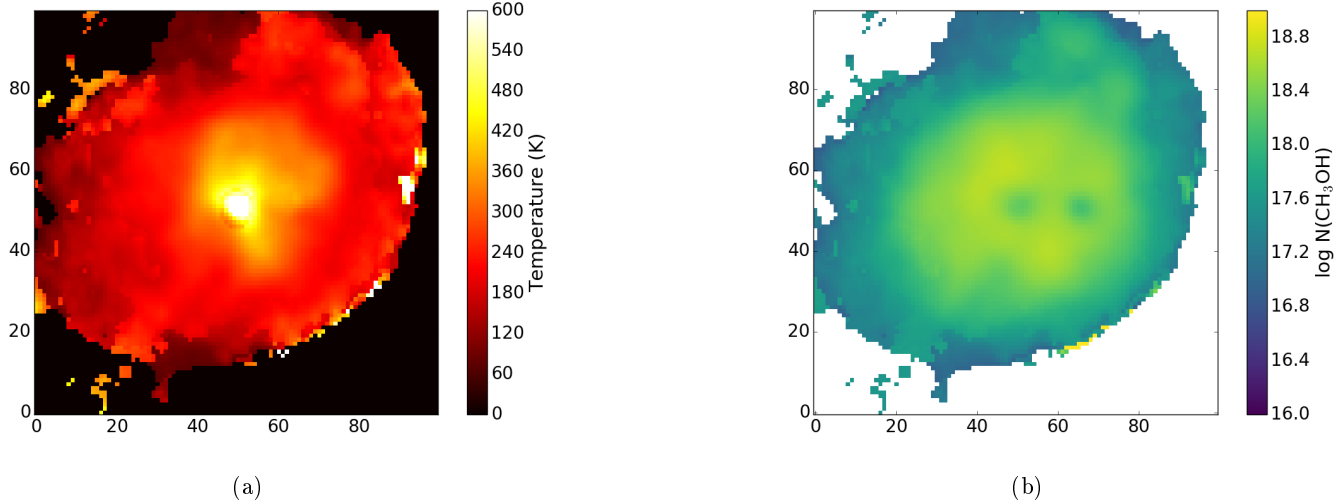


**Fig. 14.** Methanol temperature and column density maps around e2. The central regions around the cores appear to have lower column densities because the lines become optically thick and self-absorbed.

rate - onto these sources. While we cannot yet make that limit quantitative, it is clear that the HCH II region sources are accreting substantially less than the dust continuum sources.

### 3.11.2. north

The outflow from W51 north is extended and complex. A jet-like high-velocity feature appears directly to the north of W51 north in both CO and SO (Figure 23). However, in SO, this feature begins to emit at  $\sim 47 \text{ km s}^{-1}$  and continues to  $\sim 100 \text{ km s}^{-1}$ . The CO emission below  $< 70 \text{ km s}^{-1}$  is completely absent, presumably obscured by foreground material. The blueshifted component, by contrast with the red, points to the southeast and is barely detected in CO, but again cleanly in SO. It is sharply truncated, extending only  $\sim 1''$  ( $\sim 5000 \text{ AU}$ ). Unlike the Lacy jet, there is no evidence that this outflow transitions into an externally ionized state.

The northernmost point of the W51 North outflow may coincide with the Hodapp & Davis (2002) H<sub>2</sub> and [Fe II] outflow. There is some CO 2-1 emission coincident with the southernmost point of the H<sub>2</sub> features, and these all lay approximately along the W51 North outflow vector. However, the association is only circumstantial.

### 3.11.3. The e2e outflow

The dominant outflow in W51, which was previously detected by the SMA (Shi et al. 2010b,a), comes from the source e2e. This outflow is remarkable for its high velocity, extending nearly to the limit of our spectral coverage in <sup>12</sup>CO. The ends of the flow cover at least  $-50 < v_{lsr} < 160 \text{ km s}^{-1}$ , or a velocity  $v \pm 100 \text{ km s}^{-1}$ .

The morphology is also notable. Both ends of the outflow are sharply truncated at  $\sim 2.5''$  (0.07 pc) from e2e (Figure 24). To the southeast, the high-velocity flow lies along a line that is consistent with the extrapolation from the northwest flow, but at lower velocities ( $10 < v_{LSR} < 45 \text{ km s}^{-1}$ ), it jogs toward a more north-south direction (Fig-

ure 25). In the northwest, the redshifted part of this flow ( $70 < v_{LSR} < 120 \text{ km s}^{-1}$ ) apparently collides with a blueshifted flow from another source ( $22 < v_{LSR} < 45 \text{ km s}^{-1}$ ), suggesting that these outflows intersect, though such a scenario seems implausible given their small volume filling factor.

The extreme velocity and morphology carry a few implications for the accretion process in W51. The sharp symmetric truncation, combined with the extraordinary velocity, suggests that the outflow is freshly carving a cavity in the surrounding dense gas. The observed velocities are high enough that their bow shocks likely dissociated all molecules, so some ionized gas is likely present at the endpoints; this ionized gas has not been detected in radio images because of the nearby 100 mJy HCHII region e2w. The dynamical age of the outflow is  $\sim 600$  years at the peak observed velocity, which is a lower limit on the true age of the outflow.

### 3.11.4. e8

There are at least four distinct outflows coming from the e8 filament. The e8 core is launching a redshifted outflow to the northwest. A blueshifted outflow is coming from somewhere south of the e8 peak and pointing straight east. While these originate quite near each other, they seem not to have a common source, since the red and blue streams are not parallel (Figures 24 and 26). The e8 outflows are too confused and asymmetric for simple interpretation.

## 4. Discussion

### 4.1. The scales and types of feedback

The most prominent features of our observations are the warm, chemically enhanced regions surrounding the highest dust concentrations, and the corresponding lack of such features around the ionized nebulae. This difference implies that the immediate star formation process - that of gas collapse and fragmentation from a molecular cloud - is primar-

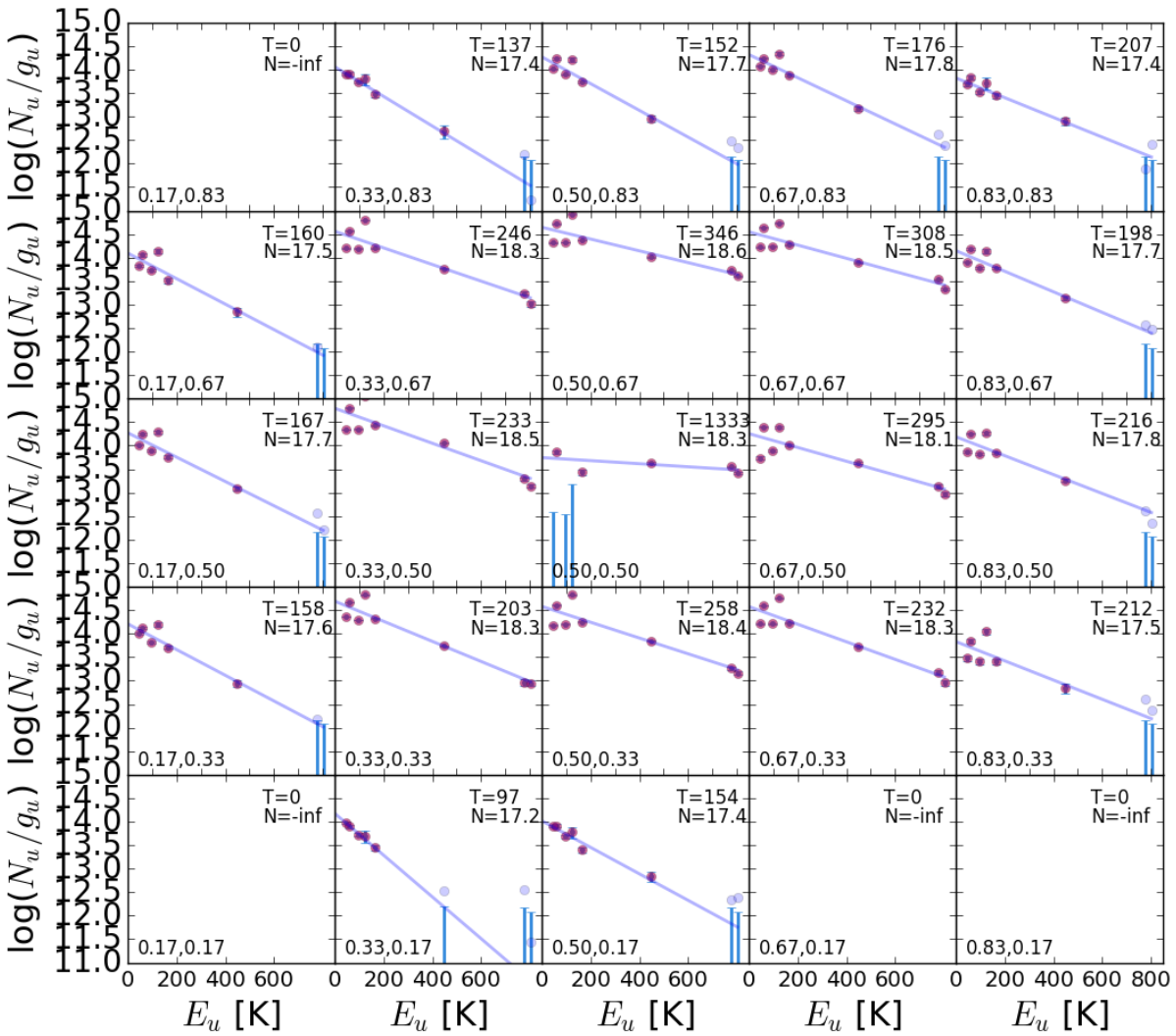


**Fig. 15.** A sampling of fitted rotation diagrams of the detected CH<sub>3</sub>OH transitions. These are meant to provide validation of the temperatures and column densities derived and shown in Figure 14. The lower-left corner shows the position from which the data were extracted in that figure in units of figure fraction. The horizontal black lines show the detection threshold of each of the transitions; points below these lines are ignored when fitting, and instead the threshold itself is used. The fitted temperature and column are shown in the top right of each plot.

ily affected by feedback from other forming stars, *not* from previous generations of now-exposed stellar photospheres.

On the scales relevant to the fragmentation process, i.e., the  $\sim 0.1$  pc scales of prestellar cores, this decoupling can be explained simply. Stellar light is produced mostly in the UV, optical, and near-infrared. As soon as a star is exposed, either by consuming or destroying its natal core, that light is able to stream to relatively large ( $\gtrsim 1$  pc) scales before being absorbed. At that point, the stellar radiation is poorly coupled to the scales of direct star formation. By contrast, stars embedded in their natal cores will have all of their light reprocessed from UV/optical/NIR to the far-IR within a  $< 0.1$  pc sphere, providing a far-infrared background light capable of heating its surroundings.

The different effects of ionizing vs thermal radiation can be seen directly in the three main massive star forming re-

gions, e2, e8, and north. Figures 20 and 21 show both the highly-excited warm molecular gas in color and the free-free emission from ionized gas in contours. As described in Section 3.10, the spatial differences indicate that the ionizing radiation sources - the exposed OB stars - have little effect on the star-forming collapsing and fragmenting gas.

The low impact of photospheric radiation on collapsing gas suggests that second-generation star formation is relatively unaffected by its surroundings. Instead, the stars of the same generation - those currently embedded and accreting - have the dominant regulating effect on the gas. The formation of the stellar initial mass function *within clusters* is therefore predominantly self-regulated, with little external influence.

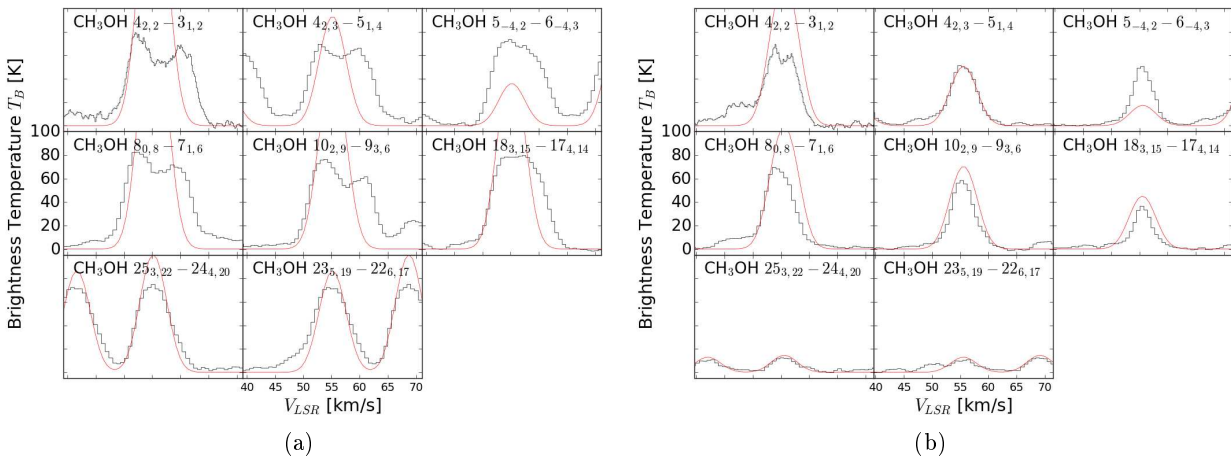


**Fig. 16.** Spectra of the CH<sub>3</sub>OH lines toward a pair of selected pixels just outside of the e2e core. (a) is 0.55'' and (b) is 1.33'' from e2e. The red curves show the LTE model fitted from a rotational diagram as shown in Figure 15. The model is not a fit to the data shown, but is instead a single-component LTE model fit to the integrated intensity of the lines shown. As such, the fit is not convincing, and it is evident that a single-temperature, single-velocity model does not explain the observed lines. Nonetheless, a component with the modeled temperature is likely to be present in addition to a cooler component responsible for the self-absorption in the low-J lines. (a) shows a pixel close to the center of e2e, which is probably optically thick in most of the shown transitions, while (b) shows a better case where the highest- $A_{ij}$  lines are overpredicted but many of the others are well-fit.

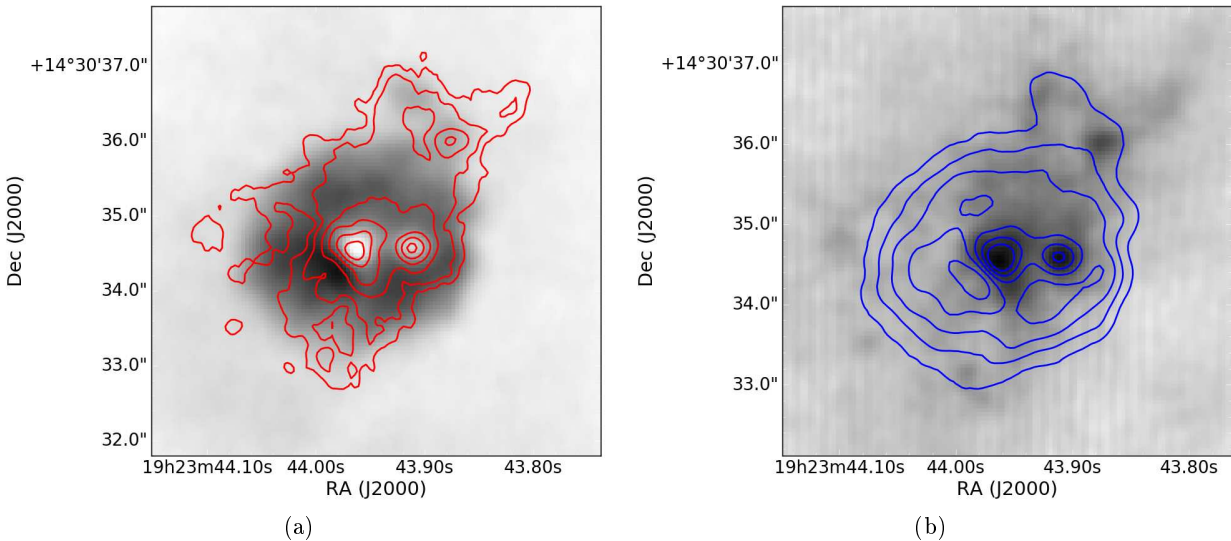


**Fig. 17.** Images showing CH<sub>3</sub>OH 10<sub>2,9</sub> – 9<sub>3,6</sub> and 225 GHz continuum emission, with CH<sub>3</sub>OH in grayscale and continuum in contours (left) and continuum in grayscale, CH<sub>3</sub>OH in contours (right). The fainter (whiter) regions in the center of the CH<sub>3</sub>OH map correspond to the bright continuum cores and show where all lines appear to be self-absorbed.

#### 4.1.1. Hot core chemical structure

In Section 3.8, we showed regions with enhanced emission in a variety of complex chemical species over a large volume. While it is not generally correct to conclude that enhanced emission indicates enhanced abundance, the additional analysis of the  $\text{CH}_3\text{OH}$  abundance in Section 3.9 suggests that there is a genuine enhancement in complex chemical abundances toward these hot cores.

We have not performed a detailed abundance analysis of multiple species, but we nonetheless suggest that these sharp-edged bubbles around the hot cores represent sublimation zones in which substantial quantities of grain-processed materials are released into the gas phase. The relatively sharp edges likely reflect the particular point where

the temperature exceeds the sublimation temperature for each species.

Most of the lines identified in the hot cores e2e, e8, and north are also present in ALMAmm14. However, their extent is greater toward the more luminous sources. An examination of the relationship between the luminosity of the protostars and the extent of their chemically enhanced zones will be useful for identifying further very massive protostars.

#### 4.1.2. Outflows

While the outflows described in Section 3.11 are impressive and plentiful, they are obviously not the dominant form of feedback, as their area filling factor is small compared to

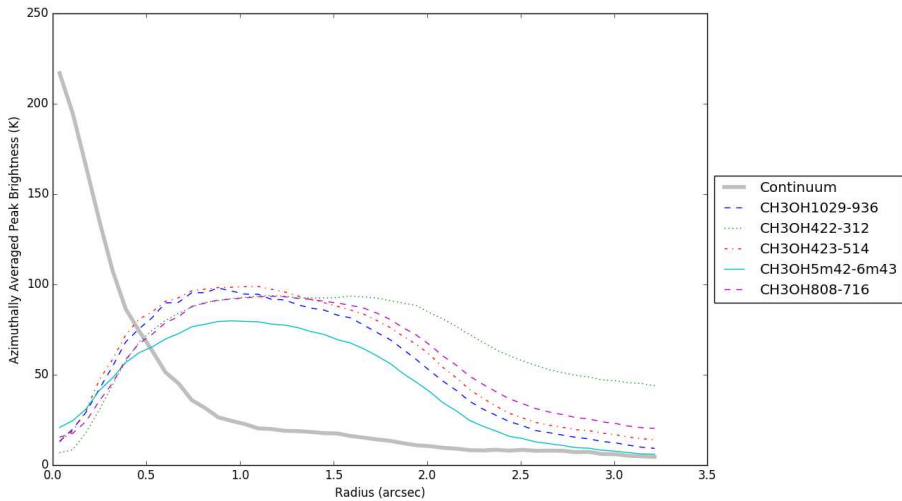


**Fig. 18.** Radial profiles of the peak surface brightness of five CH<sub>3</sub>OH transitions along with the profile of the continuum brightness. The radial profiles were constructed from images with 0.2'' resolution including only 12m data. The central dip shows where the lines go into absorption, though they are only seen in absorption at  $\sim 55 \text{ km s}^{-1}$ . The CH<sub>3</sub>OH lines are continuum-subtracted.

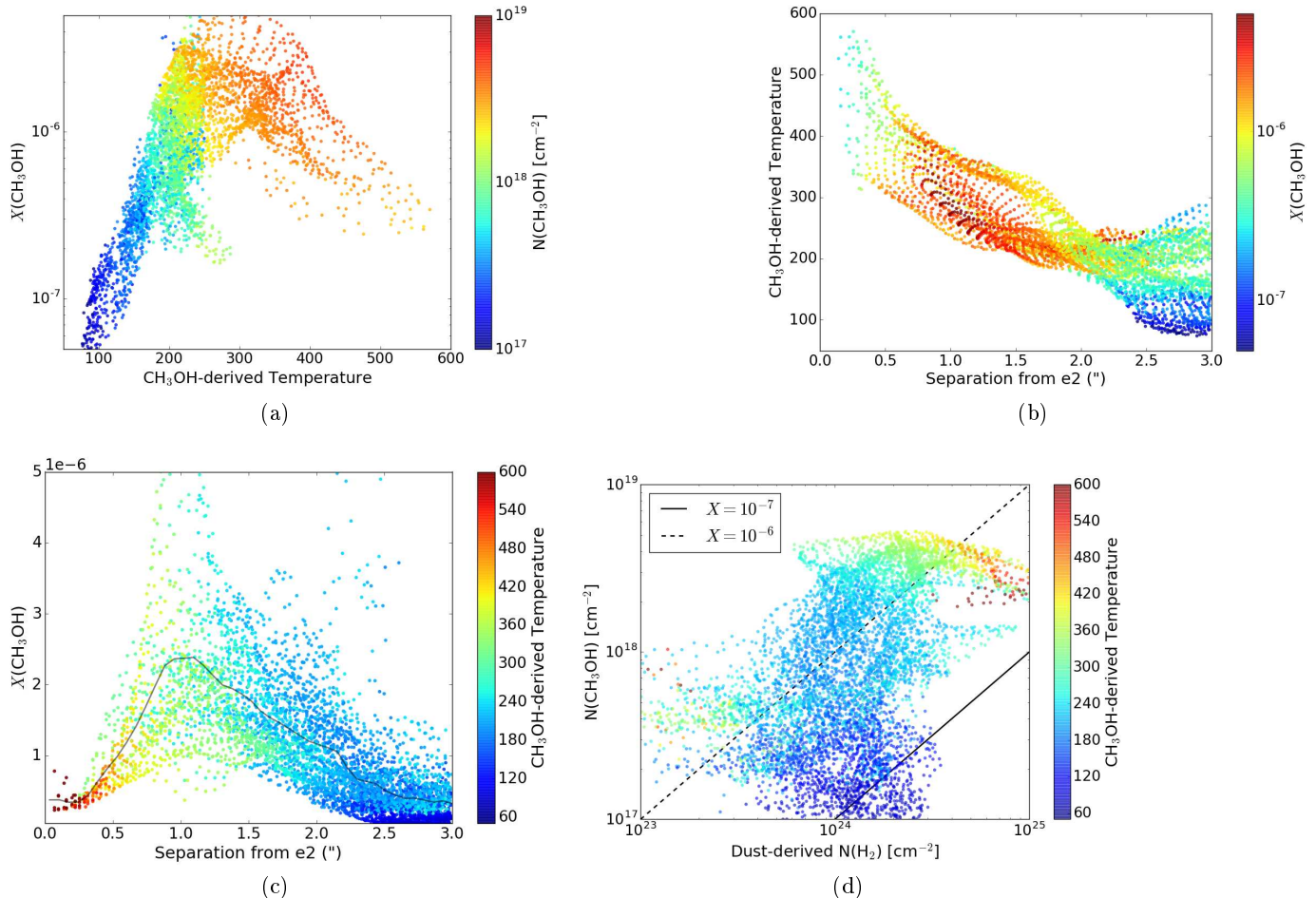


**Fig. 19.** Comparison of the CH<sub>3</sub>OH temperature, column density, and abundance. (a) The relation between temperature and abundance. There is a weak correlation, but most of the high abundance regions are at high temperatures. (b) Temperature vs distance from e2e. There is a clear trend toward higher temperatures closer to the central source (c) Abundance vs distance from e2e. The apparent dip at  $r < 1''$  is somewhat artificial, as it is driven by a rising dust emissivity that corresponds to an increasing optical depth in the dust. The CH<sub>3</sub>OH column in this inner region is likely to be underestimated. (d) CH<sub>3</sub>OH vs dust column density.

that of the various forms of radiative feedback. A low area filling factor implies a substantially smaller volume filling

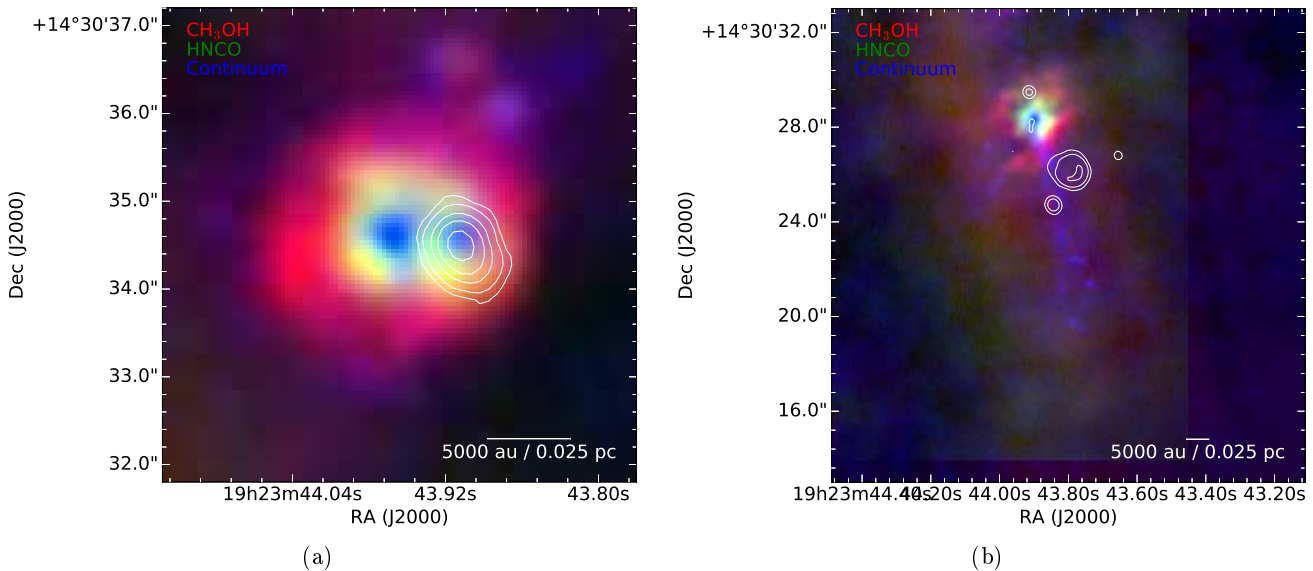


**Fig. 20.** Image of  $\text{CH}_3\text{OH}$   $80_{,8} - 71_{,6}$  (red), HCNO  $10_{,0,10} - 90_{,9}$  (green), and 225 GHz continuum (blue) toward (a) W51e2 (b) W51e8. The contours show Ku-band radio continuum emission tracing the H II regions (a) W51 e2w and (b) W51e1, e3, e4, e9, and e10. The  $\text{CH}_3\text{OH}$  emission is relatively symmetric around the high-mass protostar W51 e2e and the weak radio source W51 e8, suggesting that these forming stars are responsible for heating their surroundings. By contrast, the H II regions do not exhibit any local molecular brightness enhancements (except e8), indicating that the H II regions are not heating their local dense molecular gas.

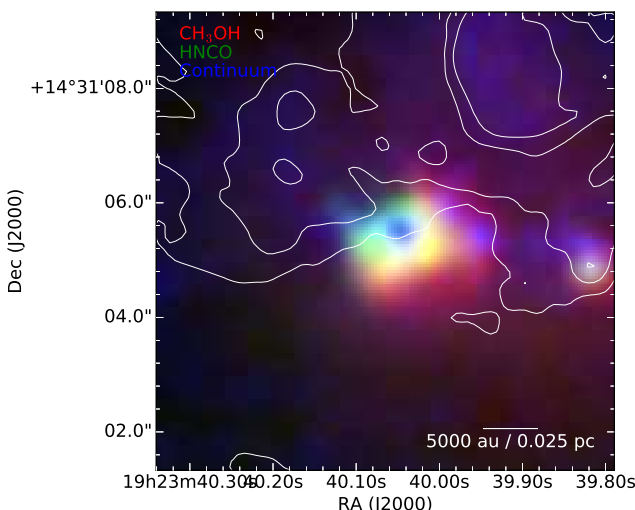


**Fig. 21.** Image of  $\text{CH}_3\text{OH}$   $8_{0,8} - 7_{1,6}$  (red), HCNO  $10_{0,10} - 9_{0,9}$  (green), and 225 GHz continuum (blue) toward north, as in Figure 20. The contours show Ku-band radio continuum emission tracing the diffuse IRS 2 H II region.

factor and therefore a lower overall effect on the cloud. However, these outflows likely do punch holes through protostellar envelopes and the surrounding cloud material, allowing radiation to escape.

The detection of widespread high-J CH<sub>3</sub>OH emission around the highest-mass protostars suggests that the use of CH<sub>3</sub>OH as a bulk outflow tracer as suggested by [Kris-tensen & Bergin \(2015\)](#) is not viable in regions with forming high-mass stars. While mid-J CH<sub>3</sub>OH emission is detected associated with the outflow (e.g., the J=10-9 transition), it is completely dominated by the general ‘extended hot core’ emission described in Section 3.8.

#### 4.2. The accreting phase of high-mass star formation

The strong outflows observed around the highest-mass forming stars, e2e, e8, and north are clear indications of ongoing accretion onto these sources. However, the bright H II regions, including e2w, e1, and d2, all lack any sign of an outflow or a surrounding rotating molecular structure. Most of these sources lack any surrounding molecular material at all.

Some models of high-mass star formation suggest that accretion continues through the ionized (H II region) phase (Keto 2007). The lack of molecular material around the majority of the compact H II regions in W51 suggests instead that most of the accretion is done by the time an H II region ignites.

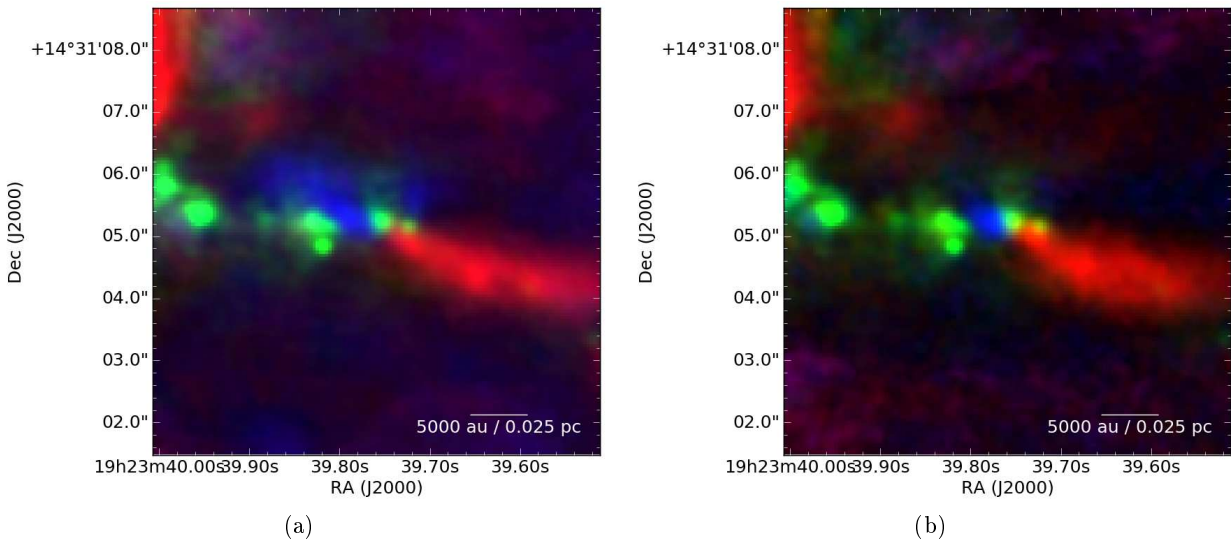


**Fig. 22.** Outflows shown in red and blue for (a) CO 2-1 and (b) SO 65 – 54 with continuum in green. This symmetric molecular outflow forms the base of the [Lacy et al. \(2007\)](#) ionized outflow detected further to the east. The continuum source is offset from the line joining the red and blue outflow lobes.

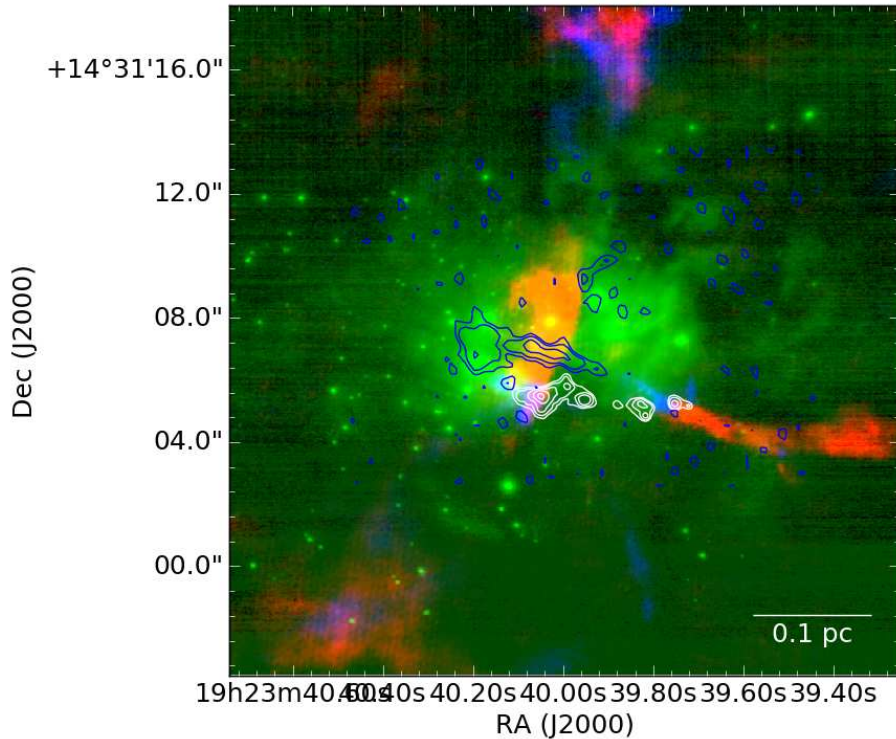


**Fig. 23.** Outflows in the W51 IRS2 region. The green emission is NACO K-band continuum (Barbosa et al. 2008), with ALMA 1.4 mm continuum contours in white and H $77\alpha$  contours in blue. The Lacy et al. (2007) jet is prominent in H $77\alpha$ .

There is one counterexample in our sample. The source d2 is a bright, compact H II region, but it is also surrounded by a molecular enhancement. However, it does not appear to drive an outflow, so there is again no direct evidence of ongoing accretion.

The correlation of the extended hot cores with outflow-driving source suggests that the heating is either from accretion luminosity or the high accretion rate is necessary to reprocess stellar photospheric light into the infrared.

### 4.3. Fragmentation: Jeans analysis

Fragmentation is one of the critical problems in high-mass star formation. Assuming typical initial conditions for molecular clouds, with temperatures of order 10 K, gas is expected to fragment into sub-solar mass cores, preventing material from accreting onto single high-mass stars (Krumholz et al. 2015). Even after high-mass stars successfully form, further fragmentation could halt the growth of these stars and limit their final mass (Peters et al. 2010b).

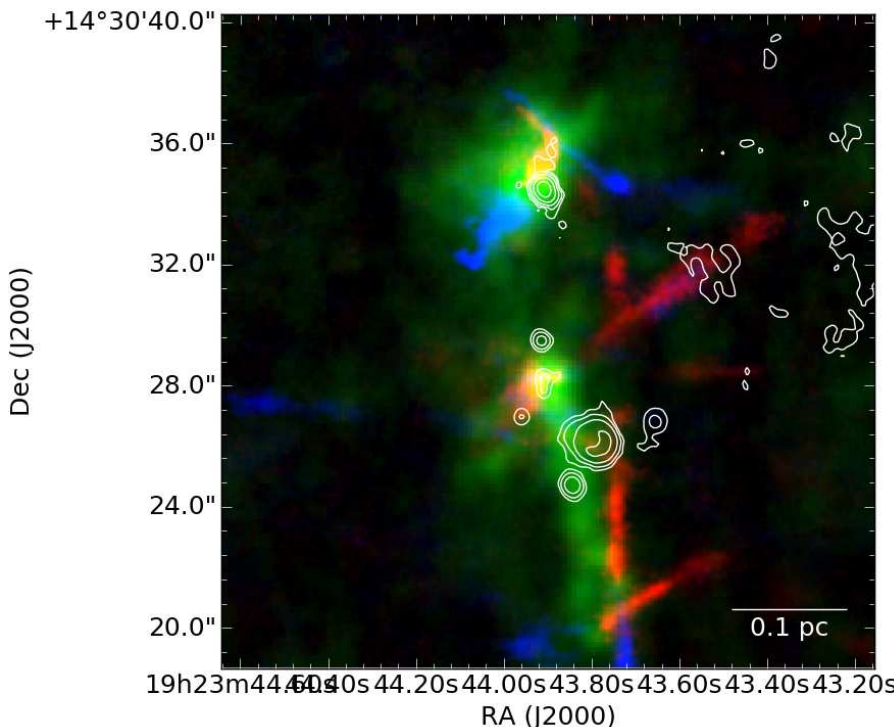


**Fig. 24.** Outflows in red and blue overlaid on mm continuum in green with cm continuum contours in white. The northern source is e2, the southern source at the tip of the long continuum filament is e8.

Thermal Jeans fragmentation can be limited or suppressed entirely if the gas is warm enough. The high observed gas temperatures,  $T \sim 100 - 600$  K over  $\sim 10^4$  AU, around the high mass protostars indicate that their radiative feedback in the infrared has a dramatic effect on the gas. The heated region qualitatively matches that of Krumholz (2006), who described a core heated only by accretion luminosity down to  $R = 10$  AU and therefore gave a lower limit on the total heating.

We examined the temperature structure around the highest-mass cores in Section 3.4 and the mass structure in Section 3.6. We put these together to measure the Jeans mass,  $M_J = (\pi/6)c_s^3 G^{-3/2} \rho^{-1/2}$ , and length,  $\lambda_J = c_s G^{-1/2} \rho^{-1/2}$ . Anyone have strong opinions about the leading numerical constants?, in Figure 27. The Jeans mass is a few times higher than the peak of the stellar initial mass function (IMF),  $M_{peak} = 0.3 M_\odot$ , implying that any fragments will be larger than the typical mass in star-forming regions. More importantly, though, the Jeans length is significantly smaller than the size scale on which it is inferred throughout the entire heated core. The gas throughout these MYSO cores is therefore Jeans-stable and will not spontaneously fragment.

The high gas temperature therefore provides a mechanism for MYSOs to avoid the “fragmentation-induced starvation” problem discussed by Peters et al. (2010b,a); Girichidis et al. (2012). Apparently, stars above some mass are able to heat hundreds of  $M_\odot$  of material surrounding them to such a degree that it cannot fragment further, providing an enormous reservoir to feed from.

Within this large reservoir, there are few currently-detected fragments. In our data, within 6500 AU of W51 north, there is only 1 (ALMAmm35), around e2e there is

the HII region e2w and possibly 2-3 others between 5000 and 6500 AU, and around e8 there are none.

Further fragmentation below 1000 AU is possible, e.g., as seen in NGC 6334Imm1 (Brogan et al. 2016). However, in the long baseline data to be presented in a future work (Goddi et al, in prep), very little additional fragmentation is observed. A few more sources are detected toward e2e and north and many toward e8, but the nature of those more compact ( $< 200$  AU) sources suggests they are protostellar or stellar. Additionally, unlike the centrally-clustered fragmentation seen in NGC 6334Imm1, the fragments appear spread out in W51. The main sources all have the majority of their flux in relatively smooth structures.

By suppressing fragmentation in their surroundings, accreting massive stars are able to sustain their mass reservoir. They effectively create their own cores. Our observations therefore support a monolithic core accretion model for the formation of massive stars, except this monolithic core is not a simple initial condition of the gas. It is not clear how such cores are assembled in the first place, but the key requirement for their formation is that a high-mass protostar must form first.

## 5. Conclusions

We have presented ALMA observations of the high-mass protocluster W51. We examined the three most massive forming stars and the surrounding population of forming stars.

The key observational results include:

- We demonstrated three techniques for estimating the temperature of dust continuum sources with ALMA: limits from dust brightness temperature, limits from line brightness temperature, and LTE modeling of CH<sub>3</sub>OH

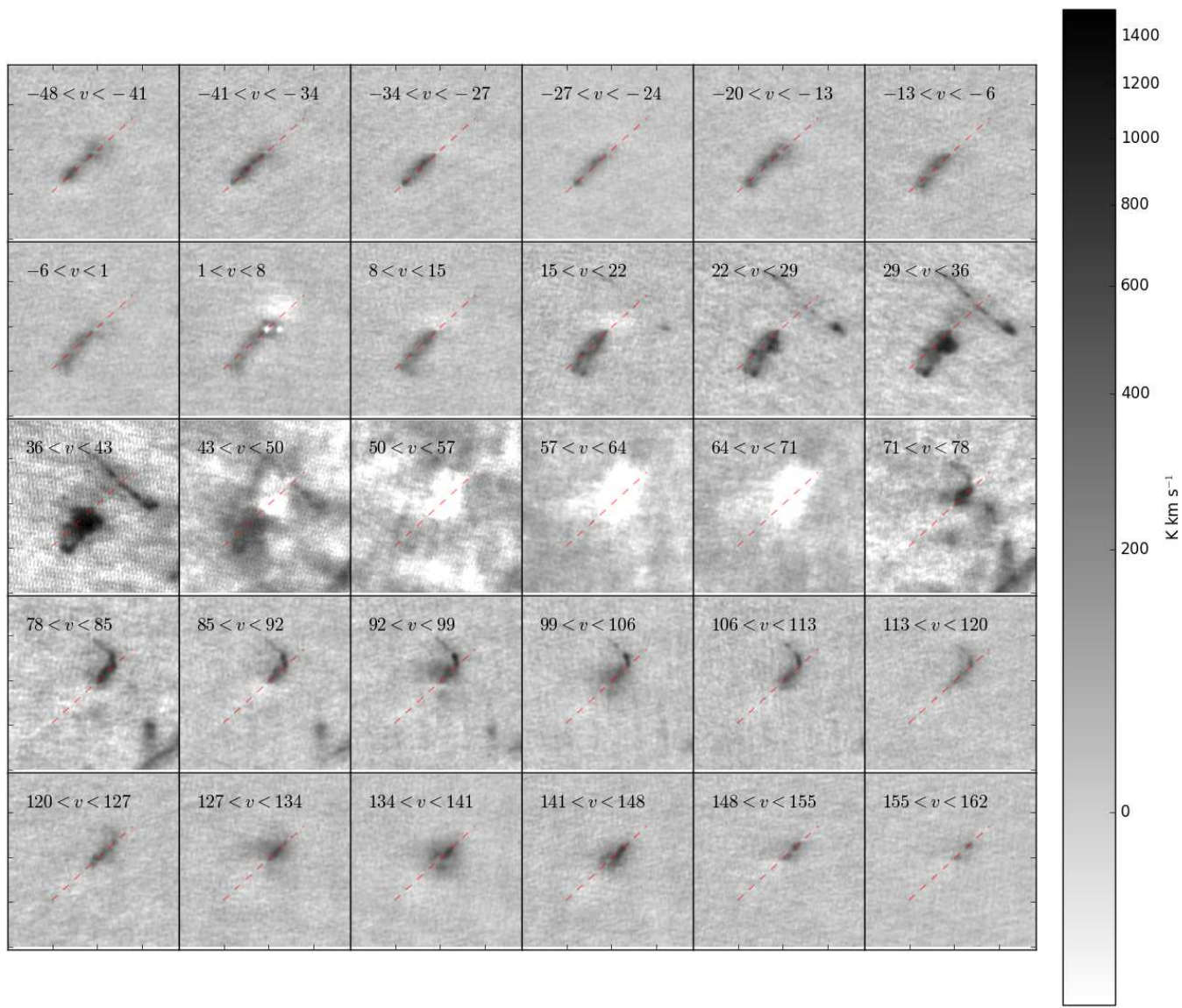


**Fig. 25.** Channel maps of the e2e outflow in CO 2-1. The dashed line approximately connects the northwest and southeast extrema of the flow.

lines. While these methods do not necessarily agree or provide direct and accurate measurements of the temperature, they provide strong enough constraints to draw substantial physical conclusions.

- We cataloged and classified 75 continuum sources on the basis of their dust emission, line emission, and morphology.
- We identified chemically enhanced regions around high-mass protostars and suggest they are desorption zones

From these observations, we have inferred the following:

- During the earliest stages of their formation, before they have ignited H II regions, high-mass protostars heat a large volume, and correspondingly large mass, of gas around them.
- Older massive stars, those with surrounding H II regions, appear to have little effect on the temperature of dense gas around them. While some are embedded within larger hot cores, they do not appear to be the main heating sources. Their luminosity must therefore

escape without being fully reprocessed into infrared radiation.

- Heated massive cores surrounding the highest-mass protostars in W51 show no evidence of ongoing fragmentation and are warm enough to suppress Jeans fragmentation. Hot massive cores therefore serve as a mass reservoir for accretion onto possibly single massive stars.

**Acknowledgments** The National Radio Astronomy Observatory is a facility of the National Science Foundation operated under cooperative agreement by Associated Universities, Inc. This paper makes use of the following ALMA data: 2013.1.00308.S and 2015.1.01596.S. ALMA is a partnership of ESO (representing its member states), NSF (USA) and NINS (Japan), together with NRC (Canada), NSC and ASIAA (Taiwan), and KASI (Republic of Korea), in cooperation with the Republic of Chile. The Joint ALMA Observatory is operated by ESO, AUI/NRAO and NAOJ.

#### Code Packages Used:

- CASA <https://casa.nrao.edu/>

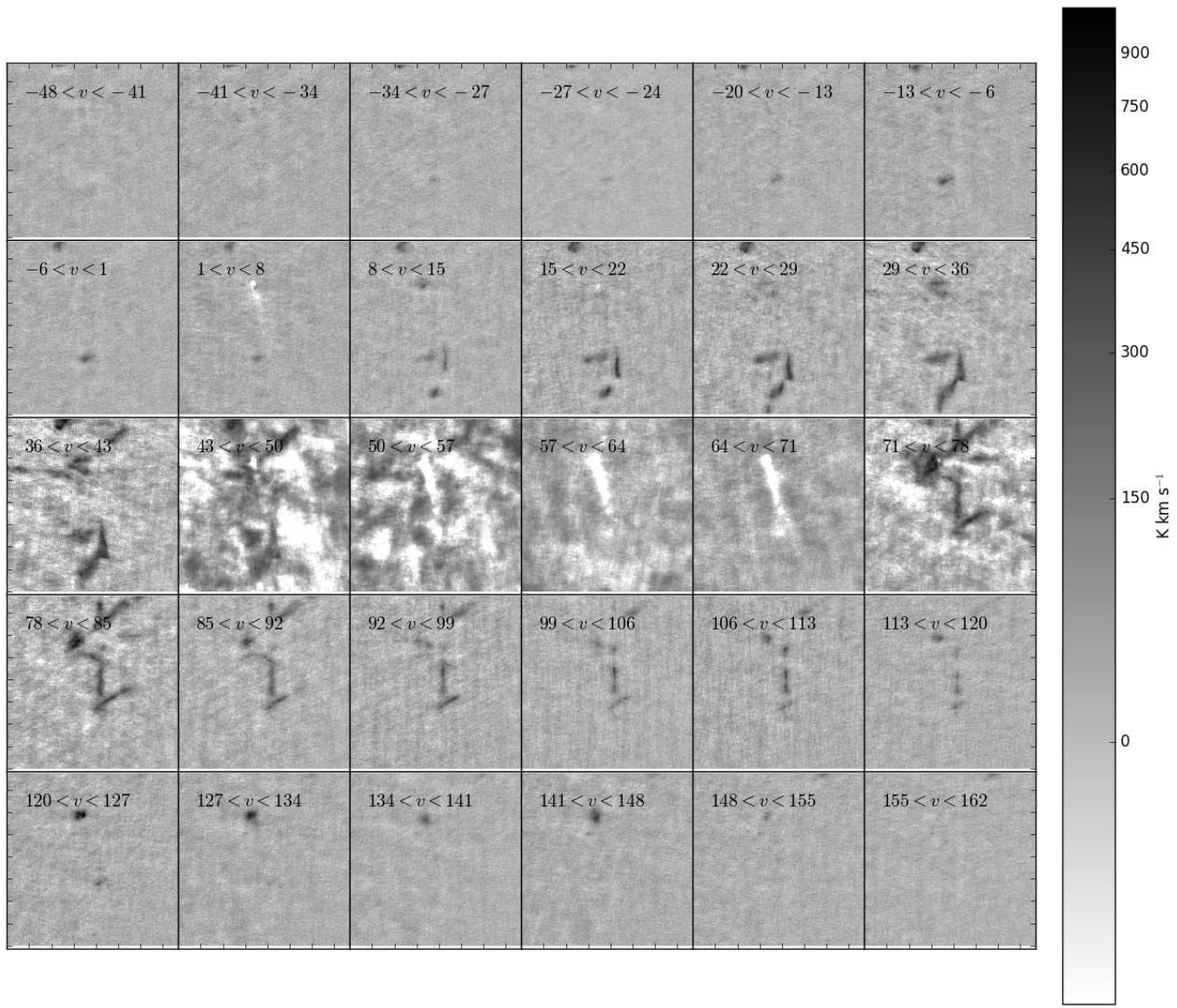


**Fig. 26.** Channel maps of the e8 outflow in  $^{12}\text{CO}$  2-1. The outflow here are more erratic, with fewer clearly-connected red and blue lobes.

- pyspeckit <http://pyspeckit.bitbucket.org> Ginsburg & Mirocha (2011)
- aplpy <https://aplpy.github.io/>
- wcsaxes <http://wcsaxes.readthedocs.org>
- spectral cube <http://spectral-cube.readthedocs.org>
- ds9 <http://ds9.si.edu>
- Forgan, D. H., Ilee, J. D., Cyganowski, C. J., Brogan, C. L., & Hunter, T. R. 2016, ArXiv e-prints
- Ginsburg, A., Bressert, E., Bally, J., & Battersby, C. 2012, ApJ, 758, L29
- Ginsburg, A. et al. 2013, ApJS, 208, 14
- 2016a, A&A, 586, A50
- 2016b, ArXiv e-prints
- Ginsburg, A. & Mirocha, J. 2011, PySpecKit: Python Spectroscopic Toolkit, Astrophysics Source Code Library
- Girichidis, P., Federrath, C., Banerjee, R., & Klessen, R. S. 2012, MNRAS, 420, 613
- Goddi, C., Ginsburg, A., & Zhang, Q. 2016
- Harvey, P. M., Joy, M., Lester, D. F., & Wilking, B. A. 1986, ApJ, 300, 737
- Hodapp, K. W. & Davis, C. J. 2002, ApJ, 575, 291
- Keto, E. 2007, ApJ, 666, 976
- Klassen, M., Pudritz, R. E., Kuiper, R., Peters, T., & Banerjee, R. 2016, ApJ, 823, 28
- Kristensen, L. E. & Bergin, E. A. 2015
- Kroupa, P. 2001, MNRAS, 322, 231
- Krumholz, M. R. 2006, ApJ, 641, L45
- Krumholz, M. R., Fumagalli, M., Silva, R. L. d., Rendahl, T., & Parra, J. 2015
- Krumholz, M. R., Klein, R. I., & McKee, C. F. 2007, ApJ, 656, 959

## References

- Aguirre, J. E. et al. 2011, ApJS, 192, 4  
 Barbosa, C. L., Blum, R. D., Conti, P. S., Damineli, A., & Figuerêdo, E. 2008, ApJ, 678, L55  
 Bate, M. R. 2012, MNRAS, 419, 3115  
 Bate, M. R., Tricco, T. S., & Price, D. J. 2014, MNRAS, 437, 77  
 Beltrán, M. T. & de Wit, W. J. 2016, A&A Rev., 24, 6  
 Brogan, C. L., Hunter, T. R., Cyganowski, C. J., Chandler, C. J., Friesen, R., & Indebetouw, R. 2016, ArXiv e-prints  
 Crowther, P. A. et al. 2016  
 De Pree, C. G. et al. 2014, ApJ, 781, L36  
 Eisner, J. A., Greenhill, L. J., Herrnstein, J. R., Moran, J. M., & Menten, K. M. 2002, ApJ, 569, 334

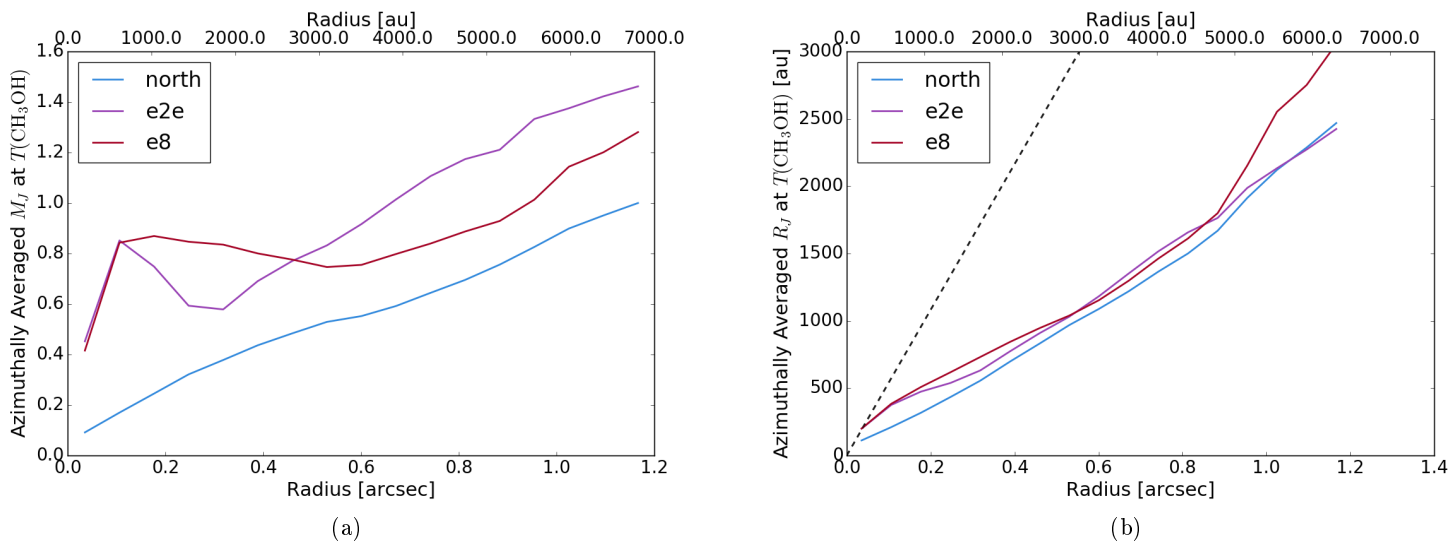


**Fig. 27.** The azimuthally averaged (a) Jeans mass and (b) Jeans length surrounding the three most massive cores. We used the CH<sub>3</sub>OH temperature from 3.9, Figure 8b in both the Jeans mass calculation and the dust-based mass determination. The Jeans mass decreases toward the center at least in part because of the density increase, while the temperature only rises slowly. In (b), the dashed black line shows the  $R_J = R$  line, below which the gas is stable to the Jeans instability.

- Krumholz, M. R., Klein, R. I., McKee, C. F., Offner, S. S. R., & Cunningham, A. J. 2009, Science, 323, 754  
 Krumholz, M. R. & Matzner, C. D. 2009, ApJ, 703, 1352  
 Krumholz, M. R., McKee, C. F., & Klein, R. I. 2005, ApJ, 618, L33  
 Kuiper, R., Turner, N. J., & Yorke, H. W. 2016  
 Kuiper, R. & Yorke, H. W. 2012, ArXiv e-prints  
 —. 2013, ApJ, 763, 104  
 Kuiper, R., Yorke, H. W., & Turner, N. J. 2015, ApJ, 800, 86  
 Lacy, J. H. et al. 2007, ApJ, 658, L45  
 Molinari, S. et al. 2016, ArXiv e-prints  
 Offner, S. S. R., Lee, E. J., Goodman, A. A., & Arce, H. 2011, ApJ, 743, 91  
 Peters, T., Banerjee, R., Klessen, R. S., Mac Low, M.-M., Galván-Madrid, R., & Keto, E. R. 2010a, ApJ, 711, 1017  
 Peters, T., Klessen, R. S., Mac Low, M.-M., & Banerjee, R. 2010b, ApJ, 725, 134  
 Rosen, A. L., Krumholz, M. R., McKee, C. F., & Klein, R. I. 2016  
 Rosolowsky, E. W., Pineda, J. E., Kauffmann, J., & Goodman, A. A. 2008, ApJ, 679, 1338  
 Sato, M., Reid, M. J., Brunthaler, A., & Menten, K. M. 2010, ApJ, 720, 1055  
 Shi, H., Zhao, J.-H., & Han, J. L. 2010a, ApJ, 718, L181  
 —. 2010b, ApJ, 710, 843  
 Sievers, A. W., Mezger, P. G., Bordeon, M. A., Kreysa, E., Haslam, C. G. T., & Lemke, R. 1991, A&A, 251, 231  
 Wang, K., Testi, L., Ginsburg, A., Walmsley, C. M., Molinari, S., & Schisano, E. 2015, MNRAS, 450, 4043  
 Yorke, H. W. & Sonnhalter, C. 2002, ApJ, 569, 846  
 Zapata, L. A., Ho, P. T. P., Schilke, P., Rodriguez, L. F., Menten, K., Palau, A., & Garrod, R. T. 2009, ApJ, 698, 1422  
 Zapata, L. A., Tang, Y.-W., & Lurini, S. 2010, ApJ, 725, 1091  
 Zhang, Q. & Ho, P. T. P. 1997, ApJ, 488, 241

## Appendix A: A bubble around e5

There is evidence of a bubble in the continuum around e5 with a radius of 6.2'' (0.16 pc; Figure A.1). The bubble is completely absent in the centimeter continuum, so the observed emission is from dust. The bubble edge can be seen from 58 km s<sup>-1</sup> to 63 km s<sup>-1</sup> in C<sup>18</sup>O and H<sub>2</sub>CO, though it is not continuous in any single velocity channel. There is a collection of compact sources (protostars or cores) along the southeast edge of the bubble.

The presence of such a bubble in dense gas, but its absence in ionizing gas, is surprising. The most likely mechanism for blowing such a bubble is ionizing radiative feedback, especially around a source that is currently a hyper-compact HII region, but since no free-free emission is evident within or on the edge of the bubble, it is at least not presently driving the bubble. A plausible explanation for this discrepancy is that e5 was an exposed O-star within the past Myr, but has since begun accreting heavily and therefore had its HII region shrunk. This model is marginally supported by the presence of a ‘pillar’ of dense material pointing from e5 toward the south.

The total flux in the north half of the ‘bubble’, which shows no signs of free-free contamination, is about 1.5 Jy. The implied mass in just this fragment of the bubble is about  $M \sim 350 M_{\odot}$  for a relatively high assumed temperature  $T = 50$  K. The total mass of the bubble is closer to  $M \sim 1000 M_{\odot}$ , though it may be lower ( $\sim 500 M_{\odot}$ ) if the southern half is dominated by free-free emission.

With such a large mass, the implied density of the original cloud, assuming it was uniformly distributed over a 0.2 pc sphere, is  $n(\text{H}_2) \approx 2 - 5 \times 10^5 \text{ cm}^{-3}$ .

To evaluate the plausibility of the HII-region origin of the bubble, we compare to classical equations for HII regions. The Strömgren radius is

$$R_s = \left( \frac{3Q_H}{4\pi\alpha_B n^2} \right)^{\frac{1}{3}}. \quad (\text{A.1})$$

For  $Q_H \sim 10^{49} \text{ s}^{-1}$ ,  $\alpha_B = 3 \times 10^{-13} \text{ cm}^3 \text{s}^{-1}$ ,  $R_s \approx 0.01 \text{ pc}$ .

The Spitzer solution for HII region expansion gives

$$R_{\text{HII}}(t) = R_s \left( 1 + \frac{7}{4} \frac{c_{\text{II}} t}{R_s} \right)^{\frac{4}{7}}. \quad (\text{A.2})$$

With  $c_{\text{II}} = 7.5 \text{ km s}^{-1}$  and  $t = 10^4 \text{ yr}$ ,  $R_{\text{HII}}(t) \approx 0.04 \text{ pc}$ , while at  $t = 10^5 \text{ yr}$ , it is  $R_{\text{HII}} \approx 0.16 \text{ pc}$ , which is compara-

ble to the observed radius ( $r_{obs} \sim 0.13 - 0.19$  pc)

Whitworth et al. 1994 give the fragmentation timescale as

$$t_{\text{frag}} \sim 1.56 \left( \frac{c_s}{0.2 \text{ km s}^{-1}} \right)^{\frac{7}{11}} \left( \frac{Q_H}{10^{49} \text{ s}^{-1}} \right)^{-\frac{1}{11}} \left( \frac{n}{10^3 \text{ cm}^{-3}} \right)^{-\frac{5}{11}} \text{ Myr} \quad (\text{A.3})$$

Plugging in our numbers gives  $t_{\text{frag}} \approx 1.0 \times 10^5$  yr, or 10× longer than the expansion time.

These values are consistent with a late O-type star having been exposed, driving an H II region, for  $\sim 10^4 - 10^5$  year, after which a substantial increase in the accretion rate quenched the ionizing radiation from the star, trapping it into a hypercompact ( $r < 0.005$  pc) configuration. The recombination timescale is short enough that the ionized gas would disappear almost immediately after the continuous ionizing radiation source was hidden. This is essentially the scenario laid out in [De Pree et al. \(2014\)](#) as an explanation for the compact H II region lifetime problem. In this case, however, it also seems that the H II region has effectively driven the “collect” phase of what will presumably end in a collect-and-collapse style triggering event.

Technically, it is possible that e5 actually represents an optically thick high-mass-loss-rate wind rather than an ultracompact HII region. For example,  $\eta$  Car would have a flux of  $\sim 0.5$  Jy at 2 cm and  $\sim 5$  Jy at 1 mm at the distance of W51. While we cannot rule out this possibility, it would render the association of e5 with the ‘bubble’ purely coincidental.

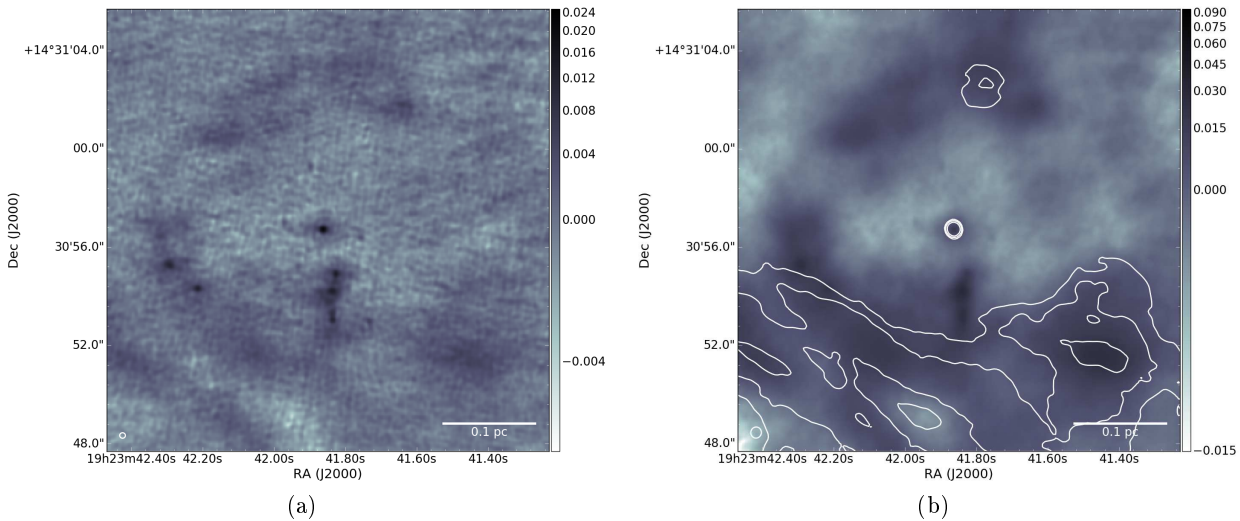


**Fig. A.1.** The bubble around source e5. The bubble interior shows no sign of centimeter emission, though the lower-left region of the shell - just south of the “cores” - coincides with part of the W51 Main ionized shell. The source of the ionization is not obvious. (*Left*): A robust -2.0 image with a small ( $0.2''$ ) beam and poor recovery of large angular scale emission. This image highlights the presence of protostellar cores on the left edge of the bubble and along a filament just south of the central source. (*Right*): A robust +2.0 image with a larger ( $0.4''$ ) beam and better recovery of large angular scales. The contours show radio continuum (14.5 GHz) emission at 1.5, 3, and 6 mJy/beam. While some of the detected 1.4 mm emission in the south could be free-free emission, the eastern and northern parts of the shell show no emission down to the  $50 \mu\text{Jy}$  noise level of the Ku-band map, confirming that they consist only of dust emission.